Measurements of oscillator strengths in V II using charge transfer reactions

Jonas Andersson

Lund Observatory
Lund University

2014-EXA82

Degree project of 60 higher education credits (for a degree of Master)
May 2014

Supervisor: Hampus Nilsson

Lund Observatory
Box 43
SE-221 00 Lund
Sweden

Abstract

Hollow cathode discharge lamps are common light sources used for branching fraction measurements. The main excitation mechanism in hollow cathodes is electron collisions and as high currents often generate much noise, lines from highly excited states of ions can be difficult to detect with high signal-to-noise ratio. In this thesis, excitations caused by selective charge transfer reactions in singly ionized vanadium has been examined by means of Fourier transform spectroscopy. Pressure and current sequences using argon, neon and krypton in a hollow cathode lamp was measured to investigate possible line enhancements caused by selective charge transfer reactions. The study presents clear evidence of overpopulation in the $(^4\mathrm{F})4d\ e^5\mathrm{P}$, $e^5\mathrm{F}$ and $e^5\mathrm{G}$ levels in singly ionized vanadium when using argon as carrier gas and the results indicate that the enhanced lines are caused by selective charge transfer reactions. As a result, 79 transition probabilities from the $(^4\mathrm{F})4d\ e^5\mathrm{P}$, $e^5\mathrm{F}$ and $e^5\mathrm{G}$ levels were derived. In addition, results in this thesis suggest that charge transfer reactions can be used as a method to experimentally derive transition probabilities of highly excited states in metal ions.

Populärvetenskaplig sammanfattning

En stor del av den information vi har om stjärnor, planeter och det interstellära mediet har erhållits genom spektroskopiska analyser. Spektroskopi innebär att man analyserar det ljusspektrum som atomer, joner eller molekyler skapar när de absorberar eller emitterar ljus med karaktäristiska energier och våglängder. Genom att analysera sådana spektra kan slutsatser dras om den gas eller plasma där absorptionen eller emissionen ägt rum. För att möjliggöra sådana slutsatser krävs en fullständig förståelse för hur ljus och atomära system interagerar med varandra och inom astrofysikalisk spektroskopi är så kallade övergångssannolikheter av särskilt intresse. Övergångssannolikheter beskriver hur sannolikt det är att en atom eller jon absorberar eller emitterar specifika våglängder och lägger därmed grunden för hur ett spektrum byggs upp.

Genom att analysera spektra från laboratorieplasman kan mätningar av dessa sannolikheter utföras. Det kan emellertid vara svårt att skapa plasman med rätta egenskaper för att kunna genomföra mätningarna vilket har resulterar i att många övergångar i joniserade metaller inte har blivit uppmätta. I detta examensarbete undersöks möjligheten att erhålla tidigare icke uppmätta övergångssannolikheter i vanadinjoner med plasman skapade i en hålkatod som är en speciell sorts ljuskälla för spektroskopiska studier. Eftersom dessa övergångssannolikheter är svåra att mäta undersöks en speciell metod för att åstadkomma lämpliga spektra genom att framkalla så kallade charge transfer reaktioner där elektroner hoppar från en atom till en jon.

Resultaten från undersökningarna visar att det är möjligt att få mycket intensivare ljus från vanadinjonerna genom att använda sig av högt tryck och låg ström i ett plasma som innehåller argon. Resultaten tyder på att effekten med stor sannolikhet kommer från charge transfer reaktioner mellan argonjoner och vanadinatomer där specifik energi frigörs och fotoner med önskvärd energi och våglängd skapas. På detta vis har 79 övergångssannolikheter i vanadinjoner blivit uppmätta. Dessutom har denna studie demonstrerat en metod för hålkatodsmätningar av övergångssannolikheter i joner som kan vara till stor nytta för astronomer världen över.

Contents

Chapter 1

Introduction

Our understanding of stars and galaxies has predominantly been obtained by observational analysis of electromagnetic spectra. Spectroscopic analysis relies on fundamental atomic parameters and to decode information in spectra, accurate data of atomic parameters such as wavelengths and oscillator strengths are required.

During the 20^{th} century, the development of quantum mechanics revealed the nature of atoms and molecules with impressive theoretical accuracy. Although theories describing atomic systems are well established, there is still information that is difficult to obtain theoretically. This is particularly true for elements with complex atomic structures. One method to experimentally derive oscillator strengths is to combine measurements of branching fractions and lifetimes. Atomic lifetimes are often measured with time-resolved laser induced fluorescence spectroscopy and branching fractions with emission spectroscopy using e.g. hollow cathode discharge lamps as light sources.

The main excitation mechanism in a hollow cathode discharge lamp is electron collisions and the rate of excitations is often dependent on the pressure and current running through the plasma. Depending on the element to study, the importance of each parameter differ but in general, pressure and current affects the number of electron collisions, the stability of the discharge and the sputtering effect.

In this thesis, an experimental investigation of singly ionized vanadium (V II) is performed to measure branching fractions of the highly excited levels in $3d^3(a^4\text{F})4d\ e^5\text{P}$, $e^5\text{F}$ and $e^5\text{G}$. The excitations are produced using a plasma created in a hollow cathode discharge lamp using argon, neon and krypton as carrier gases. Lifetime measurements of these levels have been obtained by H. Nilsson et. al. (2013) (private communication), and by combining the lifetimes with measured branching fractions, oscillator strengths are derived. As the energy required to excite the V II ions is more than 70 000 cm^{-1}, it is difficult to populate these levels by electron collisions. However, previous experiments by Johansson & Litzén (1978) have shown signatures of selective line enhancements, indicating that resonant charge transfer reactions are important in certain spectra. In their study, overpopulation in highly excited states in Fe II was caused by resonant charge transfer reactions with Ne.

To enable branching fraction measurements of the $3d^3(a^4\text{F})4d\ e^5\text{P}$, $e^5\text{F}$ and $e^5\text{G}$ levels in V II, this thesis includes an investigation of resonant charge transfer reactions to examine if the reactions can be used for controlled overpopulation in highly excited states in metal ions. This investigation examines the possible dependence on pressure, current and energy difference from level resonances between V II and the carrier gas ions.

Chapter 2

Theory

2.1 Atomic theory

Modern understanding of atoms and ions relies on the quantum mechanical treatment of such systems. The most complete theoretical description of an atomic system relies on the solution, Ψ, of the Schrödinger equation

$$H\Psi = E\Psi \tag{2.1}$$

This equation can take many forms depending on which parts that are most important to consider in the Hamiltonian. A common way to express the Hamiltonian for a multi-electron atom is

$$H = \sum_{i=1}^{N}\left(-\frac{\hbar}{2m}\nabla_i^2 - \frac{Ze^2}{4\pi\epsilon_0 r_i}\right) + \sum_{i<j=i}^{N}\frac{e^2}{4\pi\epsilon_0 r_{ij}} + \sum_{i=1}^{N}\xi(r_i)(\bar{l}_i \cdot \bar{s}_i) \tag{2.2}$$

The first summation of Eq. (2.2) corresponds to the kinetic and potential energy of the electrons in the assumed static field from the nucleus, while the second summation yields the contribution from the electrostatic repulsion between each electron pair. The third summation is the so-called spin-orbit interaction which corresponds to the potential energy related to the interaction between the spin magnetic moment and the magnetic field from the orbital motion of the electrons. For a more complete description of these systems, more terms must be included, but for the purpose of this thesis, this Hamiltonian can be considered as a valid approximation. Possible effects caused by e.g electron-nuclear interactions could however be necessary to consider, and the theoretical treatment of such finer contributions to the energy will be treated later in this chapter.

No atomic system including more than one electron can be solved analytically and the Schrödinger equation with the Hamiltonian according to Eq. (2.2) therefore relies on approximate solutions. The credibility of such approximate numerical solutions depends on the complexity of the atomic system and for atoms with complex electronic structure, experimental data for atomic parameters as energies and oscillator strengths are therefore required to evaluate the results.

2.2 Energy levels

The solution of the Schrödinger equation only allows the orbiting electrons into discrete energy levels defined by certain quantum numbers. The important quantum numbers are the principal quantum number, n, the orbital angular momentum, l and m_l. Furthermore, each electron possess an intrinsic spin s and m_s. The two quantum numbers m_l and m_s can be described as the projection of l and s, respectively, onto a defined z-axis and can take values

$$-l \leq m_l \leq l$$

$$-s \leq m_s \leq s$$

For an electron, $s = 1/2$, and m_s can thus only take the values $m_s = \pm 1/2$. The atomic configurations are defined by the principal and orbital angular momentum quantum numbers of the electron.

The general approach when calculating energy levels of multi-electron systems is to divide the part of the Hamiltonian describing the electron-electron repulsion in one radial and one tangential part (Thorne et al., 1999). The radial part can then be grouped together with the nuclear potential, resulting in an average central field dependent on r_i. The Hamiltonian in Eq. (2.2) can thus be rewritten as

$$\begin{aligned} H &= \sum_i^N H_{kin} + H_{CF} + H_{res} + H_{s-o} \\ &= \sum_i^N \left[-\frac{\hbar}{2m}\nabla_i^2 + \left[-\frac{Ze^2}{4\pi\epsilon_0 r_i} + C(r_i) \right] + \left[\sum_{j>i}^N \frac{e^2}{4\pi\epsilon_0 r_{ij}} - C(r_i) \right] + \xi(r_i)(\bar{l}_i \cdot \bar{s}_i) \right] \end{aligned} \tag{2.3}$$

where H_{CF} is the central field created by the nucleus and the electron-electron repulsion, H_{res} is the residual potential not covered in the spherically symmetric mean electron-electron repulsion potential, $C(r)$.

The method of neglecting H_{res} and H_{s-o} when solving the Schrödinger equation and treating the energy contribution from H_{res} as a perturbation to the solution defines the Russel-Saunders- or LS-coupling. The solutions give rise to ${}^{2S+1}L$-terms where L and S are eigenvalues associated with total orbital and spin angular momentum, respectively. These angular momenta are defined as

$$\bar{L} = \sum_i^N \bar{l}_i \tag{2.4}$$

$$\bar{S} = \sum_i^N \bar{s}_i \tag{2.5}$$

which corresponds to vector additions of individual electron orbital angular momentum $\bar{l}_i$ and spin $\bar{s}_i$.

If $H_{s-o} \ll H_{res}$, the energy contribution from H_{s-o} can be treated as a perturbation to the above solution. This additional perturbation will split the LS terms into so-called fine structure levels corresponding to the total angular momentum, $\bar{J} = \bar{L} + \bar{S}$. These level are described according to the extended term description

$${}^{2S+1}L_J$$

The energy difference between the fine structure levels will follow the Landé interval rule and be proportional to J.

$$E_{s-o} = \frac{A(LS)}{2}\left(J(J+1) - L(L+1) - S(S+1)\right) \tag{2.6}$$

On the other hand, if the spin-orbit interaction is much larger than the non-central electrostatic interaction, $H_{s-o} \gg H_{res}$, this reasoning breaks down. Instead, H_{res} needs to be treated as a perturbation to the H_{s-o} wave function. Consequently, the orbital and spin angular momentum of the individual electrons are coupled together to form

$$\bar{j}_i = \bar{l}_i + \bar{s}_i$$

and the resulting total angular momentum, J, is formed by

$$\bar{J} = \sum_{i=1}^N \bar{j}_i \tag{2.7}$$

This coupling scheme is known as jj-coupling and as a general rule of thumb, this coupling scheme is more valid for heavier atomic systems, while LS-coupling is appropriate for lighter atomic systems (Thorne et al., 1999).

2.3 Hyperfine structure

In addition to the fine structure levels, a new perturbation factor is introduced when considering effects from the nuclear dynamics. From the resulting angular momentum of the protons and neutrons in the nucleus, a nuclear spin $\bar{I}$ gives rise to a magnetic moment that affects the energy levels of the electrons. This magnetic moment follows the relation

$$\bar{\mu}_I = g_I \frac{e}{2m_p} \bar{I} \tag{2.8}$$

where g_I is the nuclear g-factor that can either be positive or negative and m_p the proton mass (Thorne et al., 1999). Nuclei with an even mass number have integer nuclear spin and nuclei with odd mass number have half-integer values. If both the number of protons and neutrons are even the nuclear spin is zero. The consequence of the nuclear magnetic moment and its interaction with the resulting magnetic field generated by the electrons is a perturbing term

$$H_{hfs} = -\bar{\mu}_I \cdot \bar{B}_J = C \cdot \bar{I} \cdot \bar{J}$$

which is added to the Hamiltonian. The total angular momentum of the atom becomes

$$\bar{F} = \bar{J} + \bar{I}$$

which, for atoms with spherical nuclei, leads to

$$E_{hfs} = \frac{A}{2}[F(F+1) - I(I+1) - J(J+1)] + Bf(F,I,J)$$

where A is a factor often referred to as the hyperfine structure constant and $Bf(F,I,J)$ is the contribution from electric quadrupole moments for elongated nuclei. The magnitude of $\bar{F}$, takes values between

$$F = |I-J|, |I-J|+1, ..., I+J-1, I+J$$

with the projection

$$M_f = -F, -F+1, ..., F-1, F$$

2.4 Vanadium

Vanadium is a transition group element with atomic number 23. The ground configuration of neutral vanadium is $3d^3 4s^2$ with an unfilled $d-$shell which is characteristic for transitions group elements. Vanadium has a complex energy system based on multiple parent terms, i.e. the configuration of the underlying $n-1$ electrons. Although the complexity of such atomic systems increases with the number of possible parent terms, they are important to understand the energy level structure.

Singly ionized vanadium, V^+, has the ground configuration $3d^4$ and since V III has three uncoupled d-electrons in its ground state, multiple parent terms are possible. To visualize the energy structure of V II, part of the energy level structure is presented in the term diagram in Fig. 2.1. For each electron configuration, the energy required to ionize V II, i.e. the ionization limits, depends on the parent term. As a consequence, several different ionization limits exists for V II. The lowest ionization limit corresponds to the ^{4}F term in V III, with an energy of 117 900 cm^{-1} (Kramida et al., 2013).

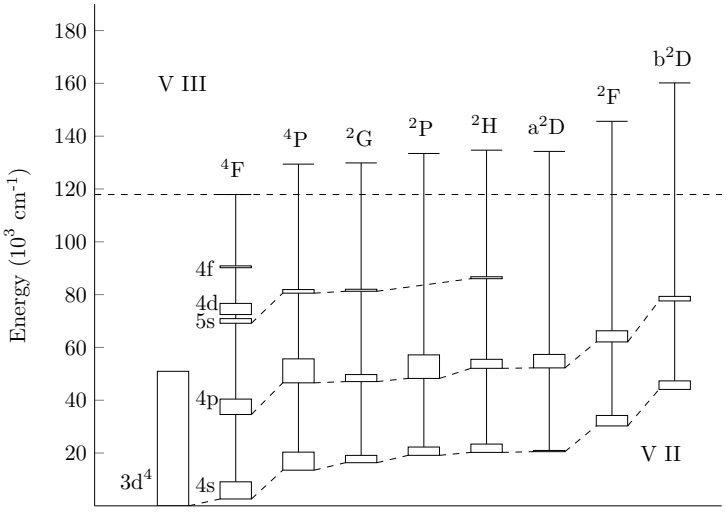

Figure 2.1: *Term structure diagram of V II. Energy levels with small energy difference are grouped together into boxes.*

2.5 Radiative transitions

The interaction between light and ions or atoms includes either an electron absorbing or emitting a photon of certain frequency. Atomic systems can therefore gain energy and become excited or relax from an excited state by interacting with a photon. The possible radiative processes are spontaneous emission, absorption and stimulated emission. Absorption describes the process when an atomic system, A, absorbs a photon of a specific frequency and becomes excited, A^*, to an energy level with energy $E_u = E_l + h\nu$ where h is Planck's constant and ν is the frequency of the photon.

$$A + h\nu \rightarrow A^* \qquad \textit{Absorption}$$

Spontaneous emission is the opposite reaction where an excited atomic system deexcites by emitting energy in form of a photon. The energy of the photon is the difference between the initial and final energy state of the system.

$$A^* \rightarrow A + h\nu \qquad \textit{Spontaneous emission}$$

Stimulated emission describes the process where an excited atomic system interacts with an incoming photon with an energy matching the difference between the excited state and a lower level. The photon may then perturb the atomic system in such way that the system relaxes to the lower level by emitting a photon of same frequency as the one perturbing the system. The process is sometimes called "inverse absorption".

$$A^* + h\nu \rightarrow A + 2h\nu \qquad \textit{Stimulated emission}$$

2.6 Selection rules

Treating the electromagnetic interaction between a photon and a bound electron with time-dependent perturbation theory, and assuming that the electromagnetic field is constant over the size of the atom, one obtains the so-called electric dipole transitions. For electric dipole transitions, certain selection rules describe which transitions are allowed. Acting with the electric dipole operator on a wave function

$$\langle \Psi_f | \, e\bar{r} \, | \Psi_i \rangle = e \int \Psi_f^* e\bar{r} \Psi_i d\bar{r} \tag{2.9}$$

it turns out that if the product of two wave functions corresponding to the final and initial states does not have odd parity, the integral will cancel when integrating for both negative and positive $\bar{r}$. This implies that for electric dipole transitions, a transformation between the initial and final state must include a change in parity. Furthermore, from the relation between parity and orbital angular momentum it follows that

$$\Delta l = \pm 1$$

$$\Delta m_l = 0, \pm 1$$

In addition, electric dipole transitions include the restrictions of the change in total angular momentum J:

$$\Delta J = 0, \pm 1$$

$$J = 0 \rightarrow J = 0 \text{ Not allowed}$$

As the electric dipole operator does not act on the spin, it follows that for pure LS-coupling

$$\Delta S = 0$$

and

$$\Delta L = 0, \pm 1$$

$$L = 0 \rightarrow L = 0 \text{ Not allowed}$$

2.7 Radiative lifetimes

Spontaneous emission causes excited atoms to lose energy through photon emission. The average time before an excited atomic state undergoes spontaneous emission is called the radiative lifetime. Time-resolved laser induced fluorescence (TR-LIF) is a well used technique for lifetime measurements where a short laser pulse selectively excites a large number of atoms to the desired state. The excited atoms will undergo spontaneous emission and the intensity of a transition from the excited level will decay with time according to

$$I(t) \propto e^{-t/\tau_u} \tag{2.10}$$

By measuring the intensity as a function of time, and fitting the experimentally measured data with an exponential, the lifetime, τ_u, can be derived (Thorne et al., 1999).

Lifetime measurements of highly excited states in ions and atoms using TR-LIF can be difficult to perform as highly energetic excitations require high frequency photons which can be difficult to create using a laser. However, if the laser intensity is sufficient and the energy level structure favourable, two-photon excitation can used. The energy sum of two photons can thus excite the atom to a high state, via a virtual state (Thorne et al., 1999). The probability of two-photon excitations increases if the virtual level lies close to a real energy level. In addition, as the excitation process includes the intermediate virtual state, transitions between two real states with same parity becomes possible.

2.8 Oscillator strengths

The probability per unit time for an excited electron to undergo spontaneous deexcitation from the upper level u to a lower level k is described by the Einstein coefficients A_{uk}. The transition probability, the branching fraction, BF_{uk} and the radiative lifetime τ_u of the upper level are related according to

$$\tau_u = 1/\sum_{k=1}^{n} A_{uk} \tag{2.11}$$

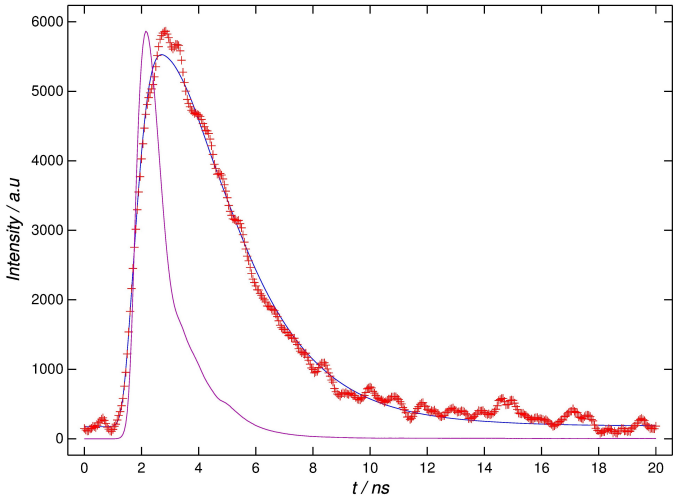

Figure 2.2: *Radiative lifetime in measurement of* $(a^4F)4d\ e^5G_6$ *in V II using two-photon laser induced florescence (LIF) technique. Image courtesy of L. Engström. The solid purple curve represents the laser, the red markers the detected signal and the solid blue curve the theoretical fit of the detected signal.*

$$BF_{uk} = A_{uk} / \sum_{k=1} A_{uk} \tag{2.12}$$

This relationship can be rewritten using the intensities of all radiative transitions from the excited level and take the form

$$BF_{uk} = I_{uk} / \sum_{k=1} I_{uk} = c_{uk} I'_{uk} / \sum_{k=1} c_{uk} I'_{uk} \tag{2.13}$$

where I is the true number of transitions per second and transition while I' is the observed intensity of each transition. The factor c is related to the calibration of the wavelength dependent response of the recording instrument. Using Eq. (2.11), (2.12) and (2.13), the relation can be rewritten as

$$A_{uk} = \frac{BF_{uk}}{\tau_u} = \frac{I_{uk}}{\tau_u \sum\limits_{k=1} I_{uk}} = \frac{c_{uk} I'_{uk}}{\tau_u \sum\limits_{k=1} c_{uk} I'_{uk}} \tag{2.14}$$

Consequently,

$$A_{uk} = f(I'_{u1}, I'_{u2}, ..., I'_{uk}, ..., I'_{un}, \tau_u)$$

and can be derived using experimentally measured intensities and the lifetime of the upper level.

Oscillator strengths are defined according to

$$f_{ku} = 1.499 \cdot 10^{-16} \frac{g_u \lambda^2}{g_k} A_{uk} \tag{2.15}$$

where g_u and g_k is the statistical weights of the upper and lower level while λ_{uk} is the wavelength of the emitted photon, described in Å.

Accurate oscillator strengths are crucial for a range of astrophysical applications. In stellar spectroscopy, the equation

$$\log \frac{\omega}{\lambda} = \log C + \log A + \log g_k f \lambda - \theta_{ex} \chi - \log \kappa_\nu \tag{2.16}$$

where ω is the equivalent width of a spectral line described as a function of a constant C, elemental abundance ratio, $A = N_E/N_H$, oscillator strength, f, inverse temperature dependence $\theta_{ex} = 5040/T_{ex}$, excitation potential χ and line opacity, κ_ν, summarises many important observational analyses (Gray, 2005).

Equivalent widths of spectral lines are often observed and indirectly yield other free parameters, as seen in Eq. (2.16). To reduce the uncertainty of such unknown free parameters, other related fix parameters, such as oscillator strengths, must be accurate. As oscillator strengths are intrinsic atomic constants that do not vary, but affect ω, it is possible to better constrict other free parameters describing stellar properties by reducing the uncertainty in relevant oscillator strengths.

2.9 Uncertainty of oscillator strengths

As with all experimental measurements, uncertainties must be taken into account. Equation (2.14), showed that the Einstein coefficients, A_{uk}, can be described as a function of measured intensities and lifetimes. If the uncertainties in measured branching fractions and lifetimes can be considered uncorrelated, the law of propagation of uncertainty can be applied to derive the resulting uncertainties in A_{uk}.

$$u_c^2(A_{uk}) = \sum_{k=1}^{n} \left(\frac{\partial A_{uk}}{\partial I_{uk}}\right)^2 u^2(I_{uk}) + \left(\frac{\partial A_{uk}}{\partial \tau_u}\right)^2 u^2(\tau_u) \tag{2.17}$$

Equation 2.17 presents the mathematical treatment of such propagation of error suggested by Sikström et al. (2002), where u corresponds to the standard uncertainties of I_j and τ_u, and u_c the combined standard uncertainties. A more thorough definition of the term standard uncertainties is given in the report by Taylor & Kuyatt (1994) as "equal to the positive square root of the estimated variance u^2". The following derivation of Eq. (2.17) was evaluated by Sikström et al. (2002) to

$$(u_{c,r}(A_{uk}))^2 = \left(\frac{u_c(A_{uk})}{A_{uk}}\right)^2 = (1-(BF)_{uk})^2\left(\frac{u(I_{uk})}{I_{uk}}\right)^2 + \sum_{j\neq k}^{n}(BF)_{uj}^2\left(\frac{u(I_{uj})}{I_{uj}}\right)^2 + \left(\frac{u(\tau_u)}{\tau_u}\right)^2 \tag{2.18}$$

where $u_{c,r}$ is the combined relative standard uncertainty.

By evaluating the first quadratic parenthesis on the right-hand side and letting the summation include $j = k$, the relation was rewritten to

$$(u_{c,r}(A_{uk}))^2 = (1-2(BF)_{uk})\left(\frac{u(I_{uk})}{I_{uk}}\right)^2 + \sum_{j=1}^{n}(BF)_{uj}^2\left(\frac{u(I_{uj})}{I_{uj}}\right)^2 + \left(\frac{u(\tau_u)}{\tau_u}\right)^2 \tag{2.19}$$

Including the calibration uncertainty, the equation becomes

$$(u_{c,r}(A_{uk}))^2 = (1-2(BF)_{uk})\left(\frac{u(I_{uk})}{I_{uk}}\right)^2 + \sum_{j=1}^{n}(BF)_{uj}^2\left(\left(\frac{u(I'_{uj})}{I'_{uj}}\right)^2 + \left(\frac{u(c_{uj})}{c_{uj}}\right)^2\right) + \left(\frac{u(\tau_u)}{\tau_u}\right)^2 \tag{2.20}$$

The law of propagation of uncertainty therefore require the standard uncertainties of both the measured intensities $u(I)$ and of the lifetime measurements $u(\tau_u)$(Sikström et al., 2002).

2.10 Charge transfer

Slow velocity collisions between ions and atoms can result in many different reactions ranging from elastic processes, such as angular deflection, to inelastic processes, such as excitations or ionizations

(Bransden & McDowell, 1992). These processes can be further divided into additional reactions, where some involve different types of charge transfer. Charge transfer reactions are processes where one or more electrons localized about the potential of one nucleus is relocated to a new nuclear potential during the collision. Much work has been done for simple atomic and ionic systems during the 20^{th} century. However, the complexity of charge transfer processes between complex multi-electron systems makes it difficult to extend the theoretical models for simple systems further.

Different theoretical descriptions and models of several important charge transfer processes has been explained in a good way in the book "Charge exchange and the Theory of Ion-Atom Collision" written by Bransden & McDowell (1992). For slow velocity collisions between ions and atoms, the orbital velocities of the electrons are much faster than the relative velocity of the two nuclei. The electron thus feel a resulting constant attraction from the two nuclei during the time of the close encounter and the two joint systems can be considered to form a pseudo-molecule with joint orbits. As the two systems do not create a real molecular bond, a certain probability for successful transfer arises when the systems separate. This probability does in general increase the stronger attraction the transferring electron feels from the nuclear potential of the incoming system.

In reality, the concept of charge transfer becomes more complicated and the level structure of the ions and atoms becomes important. The current understanding of charge transfer relies on different models and depending on the circumstances, different models are proven more or less efficient in explaining the phenomena observed. As for complex multi-electron systems interacting through charge transfer processes, the complexity grows significantly.

In studies by Johansson & Litzén (1978), it was argued that charge transfer processes could significantly influence spectra from plasmas produced in hollow cathodes. It was further suggested that depending on the energy level structure of the two colliding systems, selective overpopulation of energy levels in resonance could be possible.

Resonant charge transfer reactions between metal atoms and noble gas ions can be described according to

$$A^+ + B \rightarrow A + B^{+*} + \Delta E \tag{2.21}$$

where A corresponds a noble gas, B a metal and ΔE is the energy difference from perfect resonance. In the reaction described in Eq. (2.21), excess energy from the recombination in the noble gas is used to excite the metal ion to a resonant level and thus overpopulate the level. It was further discussed by Johansson & Litzén (1978) that the enhancement efficiency could depend on energy difference from perfect resonance, ΔE.

Figure 2.3 presents an energy level diagram where level resonances between vanadium and krypton, neon and argon are presented. As can be seen in the figure, only singly ionized argon has levels in resonance with the $(^4\text{F})4d$ levels which include the quintets relevant for this investigation. The levels in closest resonance with the levels in $e^5\text{P}$, $e^5\text{F}$ and $e^5\text{G}$ in the $(^4\text{F})4d$ configuration is the $3s^2 3p^5\ ^2\text{P}_{3/2,1/2}$ levels in Ar II. As the energy excess from the Ar recombination matches the energy between the ground state in V and the levels in $(^4\text{F})4d$ $e^5\text{P}$, $e^5\text{F}$ and $e^5\text{G}$ in V II, a possible overpopulation of these levels could be observable. As a majority of the Ar^+ ions and V atoms in a hollow cathode plasma is expected to be in respective ground state, resonant charge transfer between these systems could cause enhancement of lines originating from the levels in $e^5\text{P}$, $e^5\text{F}$ and $e^5\text{G}$ in the $(^4\text{F})4d$ configuration in V II.

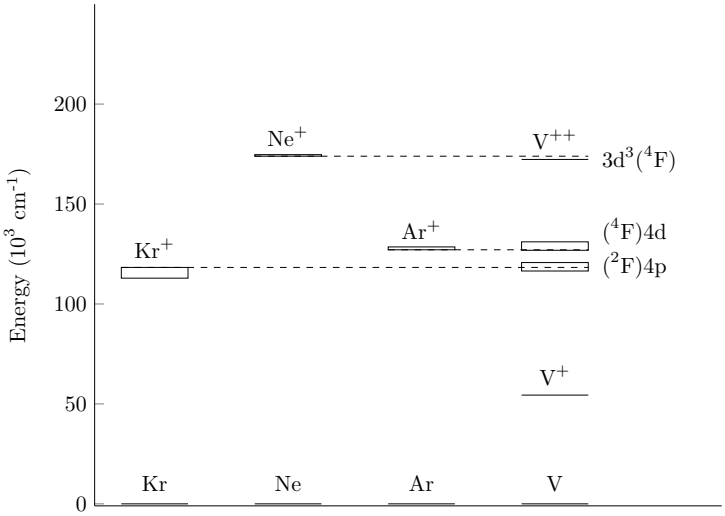

Figure 2.3: *Energy level diagram over levels in krypton, neon and argon that are in close resonance with levels in neutral, singly and doubly ionized vanadium*

Chapter 3

Experimental setup

3.1 Hollow cathode discharge lamp

To investigate electronic properties of atoms or ions using emission spectroscopy, the conditions in their environment must be such that excitations can occur. For the investigation of charge transfer processes and branching fraction measurements in V II, a hollow cathode discharge lamp, HCL, described in Fig. 3.1, was used as light source. The HCL has a cylindrical shape with two anodes and one cathode. The cathode is made out of vanadium and is located at the centre of the cylinder while the anodes are located on opposite side from the cathode. Before turning on the voltage, the HCL must be cleared from air and filled with carrier gas. In the electric field between the anodes and the cathode, free electrons are accelerated and collide with the carrier gas atoms. These collisions will ionize the gas and the positively charged ions will be accelerated and bombard the cathode. This bombardment will sputter out free atoms and ions from the cathode material into the plasma. When in the plasma, collisions from both ions and free electrons will keep the excitation processes going as long as the electric field is on. The light produced in the plasma is directed into a spectral analysis instrument.

3.2 Fourier transform spectrometer

The main principle of the Fourier transform spectrometer (FTS) presented in Fig. 3.2, is based on a Michelson interferometer. The light entering the interferometer is collimated with a lens that makes it parallel. After passing through the collimator, a beam splitter divides the light to two orthogonal paths with equal intensity. Both beams are reflected back to the beam splitter by two reflective mirrors. The beam splitter divides the two light beams once more, making two resulting paths of the light once again parallel and directed to the detector. If the path difference of the two light beams is a half integer number of the wavelengths, either completely constructive or destructive interference occurs at the detector.

Assuming that the light entering the interferometer is monochromatic with wavelength λ and thus wavenumber $\sigma = 1/\lambda$ and that the beam splitter divides the light into two equal amplitudes, a, the resulting amplitude A can be described as

$$A^2 = a^2 + a^2 + 2a^2\cos(\delta)$$

where δ is the phase shift caused by the path difference of the two beams. A phase difference of 2π means that the path difference equals $n\lambda$, which further implies that $\delta/2\pi = x/\lambda \Leftrightarrow \delta = 2\pi\sigma x$. Since the intensity of the light, I, can be described by the square of the amplitude, the expression for the intensity becomes

$$I = I_0[1 + \cos(2\pi\sigma x)]$$

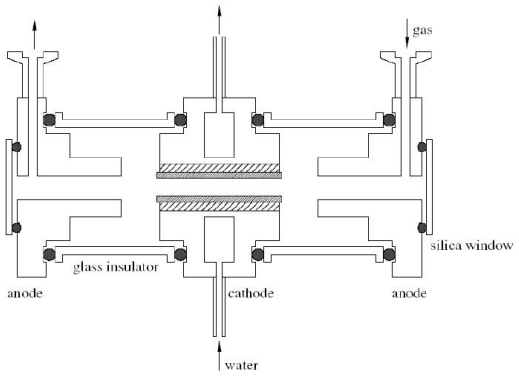

Figure 3.1: *Schematic figure of the hollow cathode discharge lamp. Courtesy of U. Litzén*

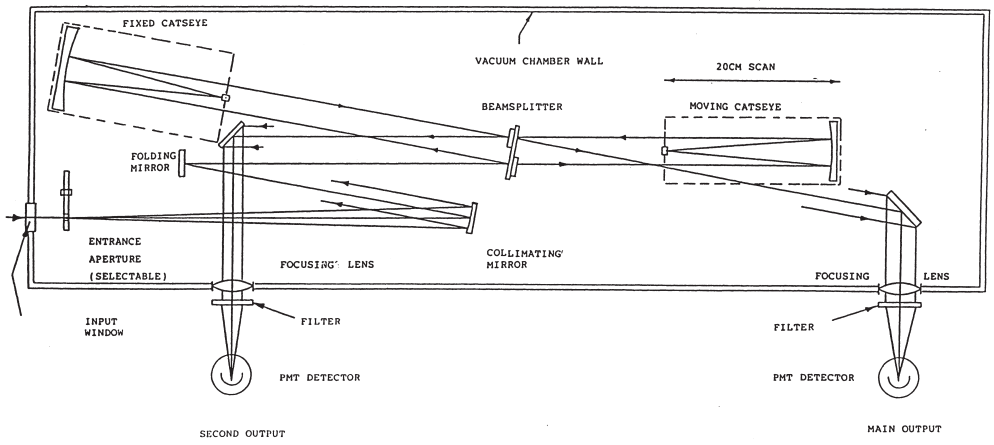

Figure 3.2: *Schematic figure of the Fourier transform interferometer.*

where $I_0 = 2a^2$ and x is the path difference. In an FTS, one of the two reflecting mirrors located after the first passage through the beam splitter is mobile. By letting the mobile mirror move and thus change the path difference of the two light beams, the image produced at the detector becomes an interference pattern as a function of the path difference.

$$I(x) = \int_{-\infty}^{\infty} B(\sigma) \cos 2\pi\sigma x \; d\sigma \tag{3.1}$$

By the inverse Fourier transform of this interferogram, the intensity as a function of wavenumber is received, which corresponds to a normal light spectrum.

3.3 Detectors

The spectral region of interest for the analysis of line enhancement from the (^{4}F)4d e^5P, e^5,F and e^5G terms in V II lies between 30000 and 45000 cm^{-1}, which corresponds to wavelengths of approximately 220 to 350 nm. This spectral region lies in the ultraviolet region of the electromagnetic spectrum. The detectors used in the experiments were photomultiplier tubes (PMT) manufactured to operate within the region between 20000 and 50000 cm^{-1}.

PMTs are vacuum tubes that rely on the photoelectric effect and secondary emission. The PMT consists of a scintillator, a photocathode and a series of dynodes, each operating under increasing potential with respect to the last. The scintillating material cause luminance when struck by photons of ionising energies. Parts of the secondary produced photons hits the photocathode and release free electrons. The electrons are focused and accelerated onto the first dynode causing emission of several secondary electrons, which are accelerated towards the second dynode. This avalanching process proceeds until the pulse of electrons is of high enough intensity to produce an electronic signal.

3.4 Sources of noise

In Fourier transform spectroscopy experiments, different sources of noise exists. Random fluctuations of light emitted from a glowing plasma can cause so-called *source noise*. Fluctuations of the light emitted from the plasma will cause false signals in the detected interferogram and these errors will propagate through the transformation to the resulting spectrum.

As the photons arriving at the detector follows the Poission distribution, the RMS of an average number of photons per second, n, will follow $\sqrt{n}$. This variation affects the photo-electrons produced in the detector and the Poission distributed photons thus induce an average current, i, that varies by $\sqrt{i}$. This source of error is referred to as *photon noise* and the resulting SNR of the detector current is

$$\text{SNR} = i/\sqrt{i} = \sqrt{i}$$

A third source of noise is *detector noise* which is produced by the detector itself. Such processes can occur from detection of spontaneously emitted electrons in the photomultiplier cathode caused by thermal processes. Detector noise can be a dominating source or noise in IR experiments but is often negligible for experiments in UV. Additional potential sources of noise can come from the electronic equipments, acoustic motions in the FTS cavity caused by imperfect vacuum and mechanical disturbances. This and further discussions about noise in FTS experiments have been described by Litzén (2003)

Chapter 4

Method

4.1 Calibration

Wavenumber calibration

To obtain accurate wavenumbers of a spectrum recorded using an FTS, wavenumber calibration of the recorded spectra is required. Inaccurately measured wavenumbers is mainly a consequence of the finite size of the aperture and from imperfect alignment of the light source and the reference beam (Salit et al., 1996). Observed wavenumbers can be corrected using the equation

$$\sigma_{\text{real}} = \sigma_{\text{obs}}(1 + k_{\text{eff}}) \tag{4.1}$$

where σ_{real} is the true wavenumber, σ_{obs} is the observed wavenumbers and k_{eff} is a correction factor that follows

$$k_{\text{eff,i}} = \frac{\sigma_{\text{real,i}}}{\sigma_{\text{obs,i}}} - 1 \tag{4.2}$$

where i is the line index. By using several lines with wavenumbers known to high accuracy, an average estimate of k_{eff} is derived. In HCL experiments, well known transitions in Ne and Ar are often used as reference when calibrating the wavenumbers.

Intensity calibration

Branching fraction measurements of excited atomic states require knowledge of the calibration factors c in Eq. (2.13). These factors relates to the response function $R(\sigma)$ according to

$$c = 1/R(\sigma) \tag{4.3}$$

The response function is the normalized function describing the detection efficiency per wavenumber of the instrument. The response of the system can be obtained by using a light source with known spectral radiance and dividing the recorded spectrum with the calibration data. The light source used to calibrate the intensities in these investigations was a deuterium discharge lamp.

To relate the recorded deuterium spectrum with the calibration data, the output and the calibration data must be described in same units. In an FTS experiment, the output signal is a wavenumber scale in relative units of photons per wavenumber interval. The calibration data must therefore be converted to photons per wavenumber interval and the recorded spectrum must be with same spectral resolution as the calibration data. The recorded spectrum from the deuterium lamp is divided point-by-point with the calibration data and the result describes the instrument's weighted wavenumber response.

4.2 Carrier gases

The choice of carrier gas depends on which element to study in the HCL but is often a noble gas. As the V II terms e^5P, e^5F and e^5G in the $3d^3(a^4F)4d$ configuration are difficult to populate by electron collisions in the HCL, the choice of carrier gas is crucial to enable branching fraction measurements. The importance of the carrier gas is to produce a stable plasma by minimizing the risk of undesired flashes and pressure fluctuations, and to sputter cathode material into the plasma. Furthermore, as suggested by Johansson & Litzén (1978) the energy structure of the metal and carrier gas atoms or ions can be important for possible charge transfer reactions. As the objective was to enable branching fraction measurements of the quintet terms e^5P, e^5F and e^5G in the $3d^3(a^4\mathrm{F})4d$ configuration, pressure and current sequences were studied to investigate relative population efficiency when using Ne, Ar and Kr as carrier gas.

Ne I and Ne II have no energy levels in resonance with the quintet levels in the V II ion and charge transfer enhancement of these transitions is therefore not expected. Although, using Ne as carrier gas can in some experiment be efficient as experiments using Ne often result in a stable discharge through the HCL for high currents. As high currents increase the number of electron collisions and increase the sputtering effect, an increased number of excitations per unit time is expected, especially for low excitations. As the electron temperature is expected to be significantly higher than the ion temperature, Boltzmann population is not expected. Higher levels are therefore generally more populated in HCL experiments than suggested by thermodynamic equilibrium.

Using Ar instead of Ne as carrier gas result in some differences. Argon has a higher atomic mass than Ne, and as a consequence, the sputtering is generally more efficient when using Ar as carrier gas and more sputtering of the cathode material increases the amount of V I and V II in the plasma. While this increases the numbers of interesting emitters, it can increase the risk of fluctuation in the discharge and the flux emitted from the plasma may not be as constant when running with high current as with Ne. Rapid time dependent flux is highly undesired as this can have negative effect on the validity of the recorded interferogram. On the other hand, the $3s^2 3p^5\ {}^2\mathrm{P}_{3/2,1/2}$ in Ar II lie in close resonance with the e^5P, e^5F and e^5G terms in V II and charge transfer effects can therefore occur (Johansson & Litzén, 1978).

As Kr has higher atomic mass than both Ne and Ar, the main motivation of using it as carrier gas was to investigate if the expected increase of sputtered cathode material increases the number of V I and V II emitters in the plasma to such extent that spectral lines from the e^5P, e^5F and e^5G terms become detectable. Charge-transfer enhancements are unlikely as no resonance between the quintet terms in V II and levels in Kr II exists.

4.3 Oscillator strenghts

The theoretical description of the experimental method to derive oscillator strengths is described in section 2.8. In short, the method requires accurate measurements of branching fractions of transitions originating from an energy level with known lifetime. Lifetime measurements of the $3d^3(a^4\mathrm{F})4d$ e^5P, e^5F, e^5G terms have been performed by H. Nilsson et al. (2013) (private communications) and are presented in Table 4.1a, 4.1b and 4.1c.

4.4 Analysis

The process from experiment to analysis is schematically described in Fig. 4.1. The mobile mirror in the FTS causes an interferens pattern of the light produced by the HCL or the calibration lamp and the resulting interferogram is detected by the PMT. To obtain the spectra, the interferogram must be Fourier transformed as described in section 3.2. This transformation was made using the

Table 4.1: *Measured lifetimes by 2-photon excitations from* $3d^3(^4F)4s\ ^5F$

(a) *Results of* $3d^3(a^4F)4d\ e^5P$

$E_u\ [cm^{-1}]$ [a]	J_u	Excitation $\lambda_{air}[nm]$ [b]	Detection $\lambda_{air}[nm]$ [c]	$\tau_{exp}\ [ns]$	$\tau_{th}\ [ns]$ [d]	$\sum A\ 10^{-8}s^{-1}$ [d]
72518	1	285.98, 286.32	283[e]	1.95 ± 0.15	2.17	4.611
72674	2	285.35, 285.68	283[e]	1.95 ± 0.15	2.39	4.191
72909	3	284.73, 285.22	280, 283[e]	1.87 ± 0.15	4.13	2.424

(b) *Results of* $3d^3(a^4F)4d\ e^5F$

$E_u\ [cm^{-1}]$ [a]	J_u	Excitation $\lambda_{air}[nm]$ [b]	Detection $\lambda_{air}[nm]$ [c]	$\tau_{exp}\ [ns]$	$\tau_{th}\ [ns]$ [d]	$\sum A\ 10^{-8}s^{-1}$ [d]
72839	1	284.68	275	1.90 ± 0.15	2.04	4.906
73027	2	284.74	261, 275	1.93 ± 0.15	2.00	5.003
73146	3	284.91	276	1.94 ± 0.15	2.00	4.986
73279	4	284.37, 285.16	262, 277	1.92 ± 0.10	2.01	4.966
73417	5	284.60	276	1.87 ± 0.10	2.03	4.924

(c) *Results of* $3d^3(a^4F)4d\ e^5G$

$E_u\ [cm^{-1}]$ [a]	J_u	Excitation $\lambda_{air}[nm]$[b]	Detection $\lambda_{air}[nm]$ [c]	$\tau_{exp}\ [ns]$	$\tau_{th}\ [ns]$[d]	$\sum A\ 10^{-8}s^{-1}$ [d]
72878	2	284.52	261, 278	1.87 ± 0.20	2.04	4.912
72951	3	284.56	276, 278	1.98 ± 0.15	2.04	4.901
73064	4	285.24	277, 279	1.80 ± 0.15	2.34	4.268
73223	5	285.38	277, 280	1.99 ± 0.15	2.05	4.868
73500	6	284.27	263	1.98 ± 0.10	2.03	4.932

[a] Ref: Kurucz (1993)
[b] Two-photon excitation using this wavelength, line width 0.01 nm.
[c] All measurements were made in the second spectral order with a line width of 0.5 nm.
[d] Semi-empirical superposition-of-configurations calculation by (Kurucz, 1993)

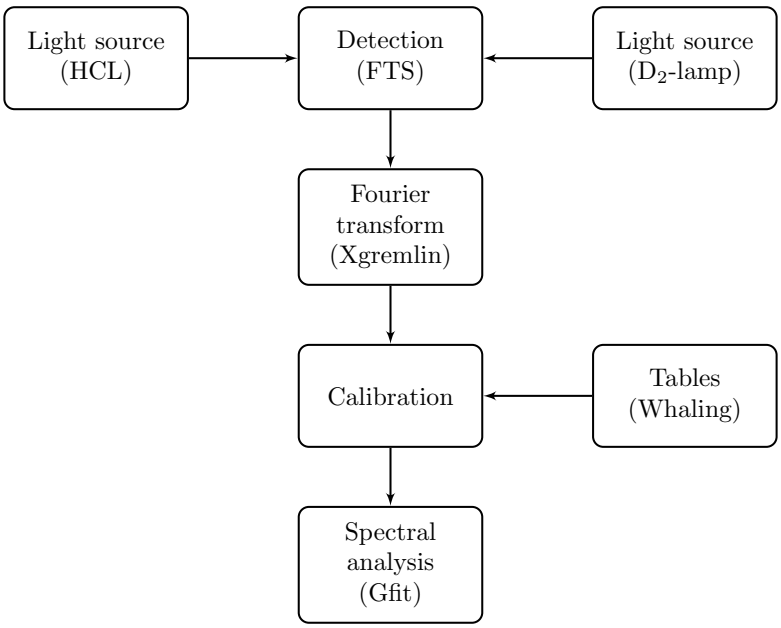

Figure 4.1: *Flow chart describing the procedure from detection to analysis of the spectral data. The detected interferogram is phase-corrected and transformed using the software Xgremlin and the calibrated data is analysed using the spectral analysis software Gfit to obtain wavenumbers, intensities FWHM and values of the uncertainty in the theoretical fits.*

software Xgremlin (Nave et al., 1997). As the recorded interferogram is not completely symmetrical, the transformation includes a non-zero imaginary part. To minimize the imaginary part, Xgremlin calculates a phase correction using manually found position for the central fringe and a phase-fit polynomial.

Before the spectral analysis, both the intensities and wavenumbers must be calibrated. The calibration procedure was performed as described in section 4.1 with the Ar II lines suggested by Whaling et al. (1995) as wavenumber standards. The calibrated data was analysed using the spectral analysis software Gfit (Engström, 1998). Gfit performes a weighted non-linear least squares fit of a sum of Gaussian, Lorentzian or Voigt functions to the measured data. The outputs from the theoretical fits calculated by Gfit are values of line positions, intensities, FWHM and χ^2 values of the uncertainty in the theoretical fits.

Chapter 5

Results

5.1 Calibration

Wavenumber calibration was performed by comparing measured Ar II lines against the reference line list presented in the work by Whaling et al. (1995). The measured Ar II lines are presented in Table 5.1 with the corresponding wavenumber standards.

Table 5.1: *Wavenumber calibration. Ar II lines*

σ_{Whaling} [cm^{-1}]	σ_{obs} [cm^{-1}]	Lower config.	J_l	Upper config.	J_u
33557.9542	33558.00031	4s	1	4p	1
33970.2358	33970.28287	4s	3	4p	3
35625.3021	35625.37031	4p	3	5s	5
36192.7931	36192.83652	4s”	2	4p”	2
36421.8504	36421.90432	3d	3	4f	5
36585.6696	36585.73988	3d	5	4f	5
38674.998	38675.07807	4p”	2	4d”	2
38892.6406	38892.71175	4p	1	4d	3
38899.0827	38899.15029	4p	3	6s	3
39018.9872	39019.03464	3d	5	5p	3
39285.8192	39285.88931	4p	3	4d	3
39420.0999	39420.15233	4p	1	6s	3
39440.4164	39440.48601	4p	3	4d	5
39958.5978	39958.64076	3d	5	5p	3

An average correction factor was calculated from each individual line correction using Eq. (4.2) to obtain a more accurate value. The derived average correction factor with one standard deviation was

$$k_{\text{eff,av}} = (-1.58 \pm 0.34) \cdot 10^{-6}$$

Intensity calibration was performed by using a standard deuterium lamp as a continuous light source and with the FTS scanning 50 scans using a resolution of 1 cm^{-1}. Figure 5.1 presents the known shape of the relative spectral radiance from the deuterium lamp, the observed shape and the resulting response function. The result presented in Fig. 5.1 must be read with caution as the y-axis presents the true scale of the response function. The data corresponding to the uncalibrated measurement and the radiance of the deuterium lamp are included with arbitrary scale to visualize wavenumber dependencies and the relative importance for the shape of the response function.

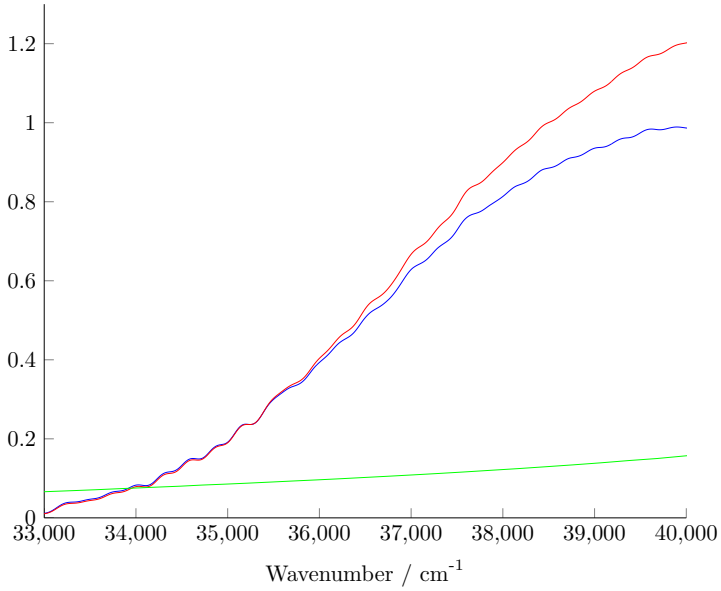

Figure 5.1: *Result from the intensity calibration. The red curve corresponds to the uncalibrated response, the green curve to the spectral radiance of the deuterium lamp and the blue curve to the calculated response function. It should be noted that the plot only presents the shape dependence on wavenumber and that the y-axis corresponds to the scale of the response function. As for the red and green curve, the y-axis is in arbitrary units.*

5.2 Line enhancements

The investigation of possible enhancement effects in the e^5P, e^5F and e^5G terms in the $(^4F)4d$ configuration of V II was performed using argon, neon and krypton as carrier gas. The investigation included analysis of line intensity variation effects from different currents and pressures in the HCL. Pressure sequences for each carrier gas and current sequences using argon and neon was measured. Current sequence measurements using Kr as carrier gas was found to cause an unstable discharge in the HCL. As the FTS is sensitive to fluctuations, no result from the attempt to measure a current sequence using krypton was obtained.

5.2.1 Current sequence

Neon

Figure 5.2 presents the results from the current sequence using neon as carrier gas. Each data point represents an average ratio between the SNR of individual lines in each experiment and the SNR of same lines in the 200 mA spectrum. The ratio average is presented with error bars corresponding to two standard deviations. The black curve corresponds to the average SNR current dependence of lines originating from the quintet terms e^5P, e^5F and e^5G in $(^4$F$)4d$ and the red curve corresponds to lines originating from levels in the $(^4$F$)4p$ configuration. Electrons deexciting from $4d$ to $4p$ will in the first deexcitation step emit photons corresponding to the intensities of the black line. In the next step, the $4p$ will deexcite and build up the red line. The SNR corresponds to the ratio of the area under the peak obtained using the line fitting software Gfit (Engström, 1998) and the RMS of the noise in the measurement. The RMS ratios of the noise are presented separately in the blue curve to illustrate the current dependence of the noise.

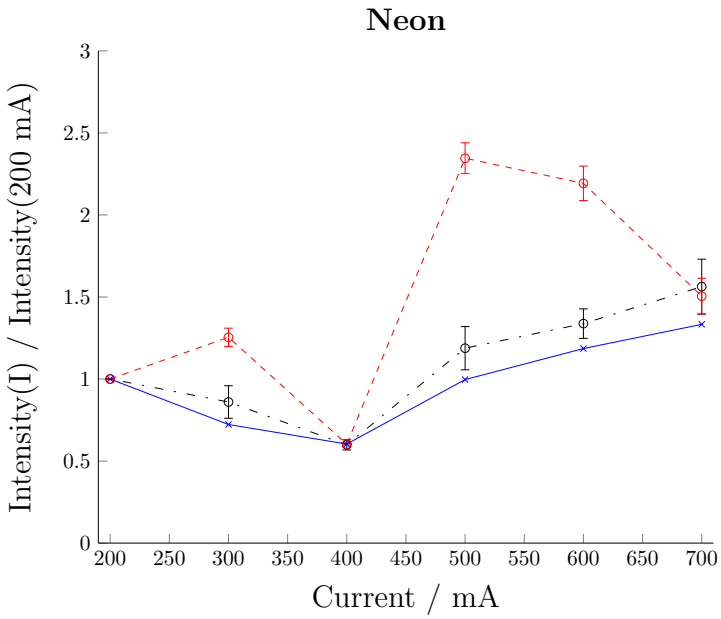

Figure 5.2: *Average intensity ratio as a function of current for lines from the highly excited levels* $(^4F)4d\ e^5P$, e^5F *and* e^5G *(dot-dashed black curve) and lower* $(^4F)4p$ *levels in same branch (dashed red curve) when using Ne as carrier gas at pressure* $P = 2$ *torr. In addition, corresponding noise ratios are presented (solid blue curve). The error bars correspond to two standard deviations of all individual line ratios used in the calculated average.*

The experiments in Fig. 5.2 was performed with constant pressure at $P = 2$ torr as this pressure kept the discharge most stable during a current sequence investigation ranging from $200 - 700$ mA. As seen in Fig. 5.2, both the red and black curve drops rapidly at 400 mA and intersects with the blue line. This suggests that the quality of the spectrum at 400 mA is poor, and most likely caused by the low quality of the plasma created in the HCL. Disregarding the experiment at 400 mA, the lines originating from the $(^4\text{F})4p$ levels rapidly increase with current up to 500 mA. This result is expected as both the sputtering effect, and the electron-ion collision rate is expected to increase with current. Increased current is however also expected to increase the noise but since the slope of the noise ratio is not obviously correlated with data in the red curve, this can not solely explain the structure of the low level intensities. As the slope of the relative noise increases linearly for $I > 400$ mA, the observed effect of decreasing SNR for $I > 400$ mA, is not caused by noise effects but rather decreased number of excitations. The black curve correlates with the RMS ratios and the observed effect is thus expected to be caused by the relative noise.

Argon

Similar results but with Ar as carrier gas are presented in Fig. 5.3. In contrast to the investigation using Ne, the most stable pressure for the sequence using Ar was $P = 1$ torr. Maximum average SNR of the lines from both the quintet levels and the $(^4\text{F})4p$ levels is found at 200 mA and the minimum is found at 500 mA. The SNR of lines from the $(^4\text{F})4p$ levels increases with current for $I > 500$ mA while lines originating from the quintets in the $4d$ levels stabilize and keep approximately a constant ratio from $400 - 700$ mA. The RMS ratio presented by the blue curve suggests that the observed average difference of the black curve between $400 - 700$ mA could be caused by noise effects as the minimum value of the RMS ratio is at 500 mA. In contrast to the results in Fig. 5.2, a significant correlation of the average SNR ratios of lines from the $4d$ levels

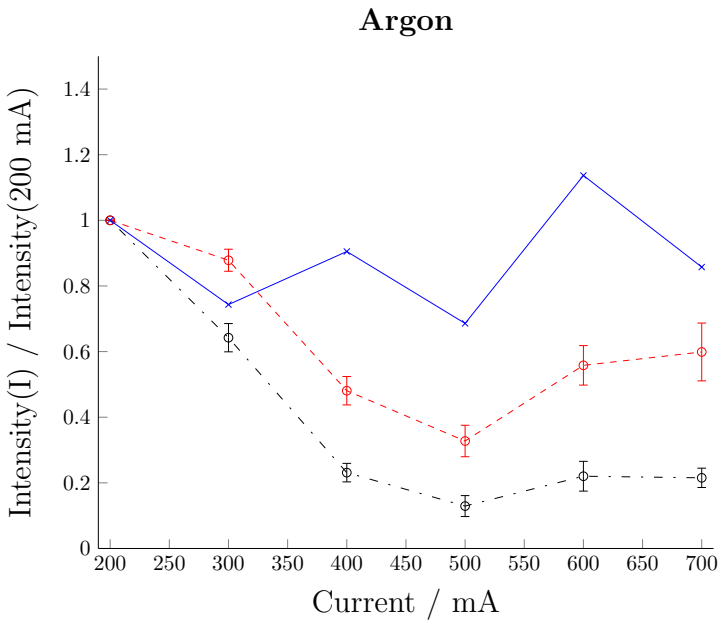

Figure 5.3: *Average intensity ratio as a function of current for lines from the highly excited levels* $(^4F)4d\ e^5P$, e^5F *and* e^5G *(dot-dashed black curve) and the lower* $(^4F)4p$ *levels in same branch (dashed red curve) using Ar as carrier gas. The current sequence was measured with* $P = 1$ *torr. The noise ratios are presented (solid blue curve) and the error bars correspond to two standard deviations.*

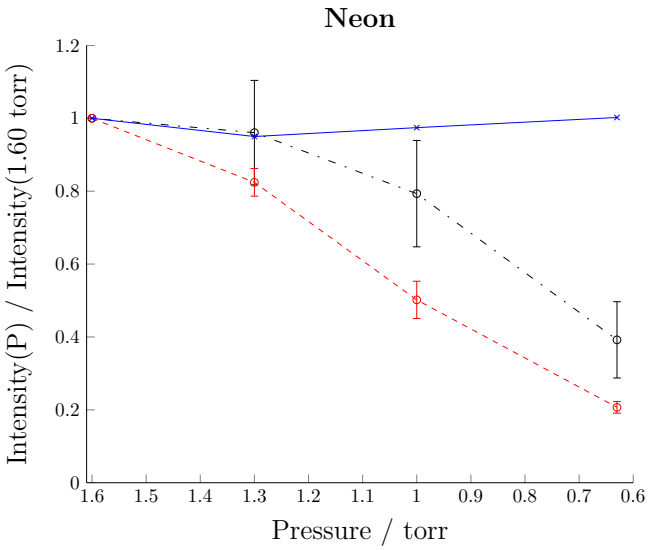

Figure 5.4: *Average intensity ratio as a function of pressure for lines from the highly excited levels* $(^4F)4d\ e^5P$, e^5F *and* e^5G *(dot-dashed black curve) and lower levels in same branch (dashed red curve). HCL is run with neon as carrier gas and* $I = 300$ *mA. The relative noise is presented (solid blue curve) and error bars correspond to two standard deviations.*

and the $4p$ levels is observed. This correlation could be an indication of overpopulation in the $4d$ quintet levels. It should be noted that as the black curve seem to stabilize for increasing currents, the correlation seem to drop as the red curve increases for $I > 500$ mA.

5.2.2 Pressure sequence

Neon

Figure 5.4 presents results from the pressure sequence analysis using Ne as carrier gas. The data are presented as for the current sequences and the average ratios of the SNR are normalized against the SNR measured in the experiment with highest pressure, $P = 1.6$ torr. The color representation of the SNR correspond to transitions from same levels as in Fig. 5.2 and 5.3. It was found that the most suitable constant current causing the most stable discharge throughout the pressure sequence was, $I = 300$ mA. It should be noted that the x-axis presents decreasing pressure to the right. As in previous plots, the bar corresponds to two standard deviations and the blue curve presents the ratio of the RMS of the noise for each individual measurement relative to the measurement at $P = 1.6$ torr.

As seen in Fig. 5.4, the RMS ratios keep an approximately constant value which suggests that no significant effect due to noise differences affects the result. The average SNR ratios of the transitions from $(^4\mathrm{F})4p$ follow a linear decrease with decreasing pressure. The SNR ratios corresponding to transitions from the $4d$ quintets show similarly a decrease with decreasing pressure. The decline of the black curve is slower than the red curve but with larger error bars.

Argon

Figure 5.5 presents the results from the pressure sequence investigation using Ar as carrier gas. The sequence is measured with constant current $I = 300$ mA, and pressure varying from 1.6 to 0.7 torr, presented with pressure decreasing to the right. The error bars show less variations about

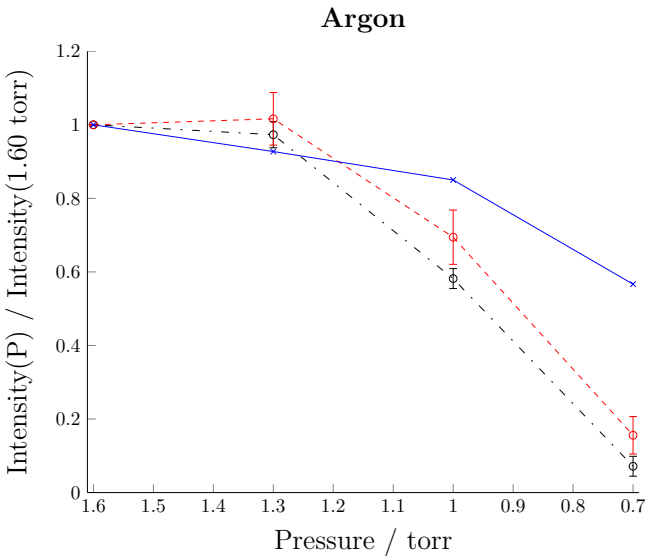

Figure 5.5: *Average intensity ratio as a function of pressure for lines from the highly excited levels* $(^4F)4d\ e^5P$, e^5F *and* e^5G *(dot-dashed black curve) and lower levels in same branch (dashed red curve). HCL is run with Ar as carrier gas and* $I = 300$ *mA. The relative noise is presented (solid blue curve) and error bars correspond to two standard deviations.*

the mean values for data representing both lines from the quintet terms e^5P, e^5F and e^5G in the $(^4\text{F})4d$ configuration and lines from the $(^4\text{F})4p$ levels. In correspondence with results from the current sequence using Ar as carrier gas, the curves of the lines originating from both the $4d$ and the $4p$ levels show a correlated dependence. The result in Fig. 5.5 indicates a clear dependency on pressure for both curves with maximum SNR for $P = 1.6$ torr. The curve representing the RMS ratios suggests that part of the pressure dependence of the SNR ratios could be caused by increased noise.

Krypton

The last pressure sequence was measured using Kr as carrier gas and as with the measurements investigating possible current dependence using krypton, difficulties arose when performing the investigations for $0.7 \leq P \leq 1.7$ torr. During the measurements, the pressure was observed to fluctuate with ± 0.5 torr, which significantly affects the recorded spectra. The pressure sequence was therefore recorded between $0.35 - 0.65$ torr with $I = 200$ mA and the result is presented in Fig. 5.6. The pressure interval and current must thus be considered when comparing the result with the sequences using Ne and Ar. Furthermore, although the pressure fluctuations were less significant, they were not eliminated. The pressure fluctuations in the measurement at 0.35 torr were significant and the result is thus affected by this.

As seen in Fig. 5.6, no error bars for the $4d$ quintet levels are included. Krypton was found to be an inefficient choice of carrier gas for excitations to the $4d$ levels and only the $(^4F)4p$ z^5F_5 - $(^4F)4d\ e^5G_6$ transition was observed through the entire sequence. The red curve, corresponding to deexcitations from $4p$, rely on a larger number of lines as these levels were more efficiently populated. The average SNR ratios of the red curve increases with a few percent for $P = 0.55$ and $P = 0.45$ relative to the experiment with $P = 0.65$, and drops at $P = 0.35$ torr. As mentioned above, the measurement at $P = 0.35$ torr included pressure fluctuations and the decrease is likely due to less sputtering or other effects causing the flux from the plasma to decrease.

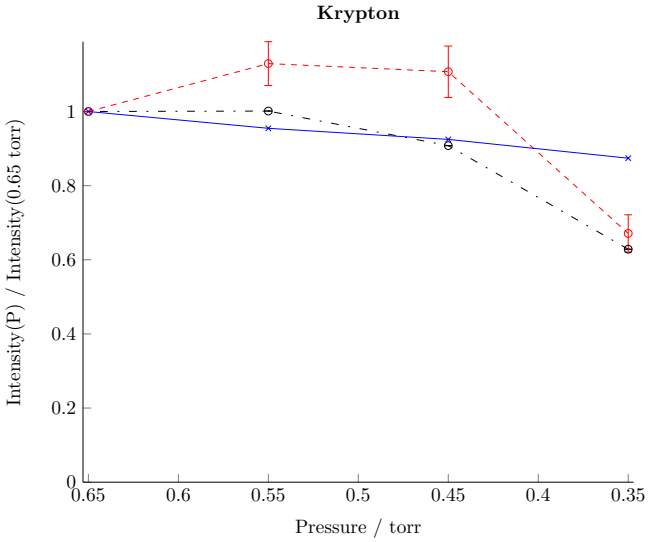

Figure 5.6: *Average intensity ratio as a function of pressure. The strongest line from the* $(^4F)4d\ e^5G_6$ *level (dot-dashed black curve) and lines from the* $(^4F)4p$ *levels (dashed red curve) is presented with the relative noise (solid blue curve). HCL is run with Kr as carrier gas and* $I = 200\ mA$.

5.2.3 Relative population

To further understand the processes causing the results presented in Fig. 5.2 to 5.6, all line intensities corresponding to transitions to and from level $(^4\mathrm{F})4p\ \mathrm{z}^5\mathrm{F}_5$ have been examined and compared to investigate the relative populations of the upper and lower levels. Figure 5.7 schematically describes how the $4d$ levels populate the intermediate $(^4\mathrm{F})4p\ \mathrm{z}^5\mathrm{F}_5$ level and deexcites further down in to lower levels. For every emitted photon caused by deexcitations to $(^4\mathrm{F})4p\ \mathrm{z}^5\mathrm{F}_5$, there is an equal number of photons emitted when the electrons deexcite a second time from $(^4\mathrm{F})4p\ \mathrm{z}^5\mathrm{F}_5$. The $(^4\mathrm{F})4p\ \mathrm{z}^5\mathrm{F}_5$ level is interesting as the majority of electrons populating this level through deexcitations from higher states originates from the $e^5\mathrm{G}$ and $e^5\mathrm{F}$ quintets of the $(^4\mathrm{F})4d$ configuration.

As measured intensities are proportional to the number of deexcited electrons, it is possible to derive a quantitative result of the number of electrons that have been excited to the higher levels and to the intermediate $(^4\mathrm{F})4p\ \mathrm{z}^5\mathrm{F}_5$ level by investigating intensities of transitions to and from $(^4\mathrm{F})4p\ \mathrm{z}^5\mathrm{F}_5$. By summing intensities from all deexcitations to $(^4\mathrm{F})4p\ \mathrm{z}^5\mathrm{F}_5$ and comparing with the summation of the intensities from deexcitations from $(^4\mathrm{F})4p\ \mathrm{z}^5\mathrm{F}_5$, it is possible to track possible overpopulations of levels above $(^4\mathrm{F})4p\ \mathrm{z}^5\mathrm{F}_5$. According to the selection rules in the section 2.6, the allowed transitions to and from $(^4\mathrm{F})4p\ \mathrm{z}^5\mathrm{F}_5$ must follow $\Delta J = 0, \pm 1$ and not $J = 0 \rightarrow J = 0$. The allowed transitions are presented in Table 5.2 and 5.3.

Although Boltzmann population is not expected in the HCL, highly excited states are expected to be significantly less populated than lower levels if electron collisions is the only excitation mechanism. If some selective populating mechanism is present, the resulting population is expected to be less energy dependent.

Table 5.2: *Deexciations to* $(^4F)4p\ z^5F_5$

Line $[cm^{-1}]$	log gf	A-value $[s^{-1}]$	E_u $[cm^{-1}]$	J_u	Upper level.
48839.150	-3.860	1.689e+04	86191.600	6.0	(2H)5s 3H
44130.700	-3.430	4.387e+04	81483.150	5.0	(2G)5s 3G
39320.500	0.086	1.397e+08	76672.950	4.0	(4F)4d 5D
38790.500	-1.849	1.579e+06	76142.950	4.0	(4F)4d 3F
38501.650	-2.196	5.724e+05	75854.100	5.0	(4F)4d 3G
38239.910	-1.578	1.983e+06	75592.360	6.0	(4F)4d 3H
37993.700	-3.370	3.734e+04	75346.150	5.0	(4F)4d 3H
36147.150	0.644	2.953e+08	73499.600	6.0	(4F)4d 5G
36064.690	0.437	2.157e+08	73417.140	5.0	(4F)4d 5F
35926.710	-0.708	1.874e+07	73279.160	4.0	(4F)4d 5F
35870.720	0.043	8.614e+07	73223.170	5.0	(4F)4d 5G
35711.080	-0.826	1.411e+07	73063.530	4.0	(4F)4d 5G
35484.970	-1.157	4.501e+06	72837.420	6.0	(4F)4d e5H
35328.250	-2.541	2.178e+05	72680.700	5.0	(4F)4d e5H
35198.640	-4.631	2.148e+03	72551.090	4.0	(4F)4d e5H
33545.980	-2.194	5.335e+05	70898.430	4.0	(4F)5s 3F
32371.690	0.133	8.631e+07	69724.140	5.0	(4F)5s 5F
32165.910	-0.758	1.339e+07	69518.360	4.0	(4F)5s 5F

Table 5.3: *Deexciations from* $(^4F)4p\ z^5F_5$

Line $[cm^{-1}]$	log gf	A-value $[s^{-1}]$	E_l $[cm^{-1}]$	J_l	Lower level.
37013.240	-0.380	3.463e+07	339.210	4.0	3d4 a5D
34384.230	-0.500	2.267e+07	2968.220	4.0	(4F)4s a5F
34189.650	0.390	1.740e+08	3162.800	5.0	(4F)4s a5F
28254.640	-1.660	1.059e+06	9097.810	4.0	(4F)4s a3F

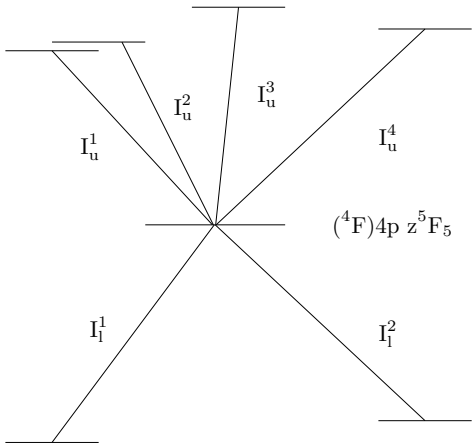

Figure 5.7: *Schematic figure of the transition channels to and from the intermediate* $(^4F)4p\ z^5F_5$ *level.*

The intensities of all transitions to and from (^{4}F)4p z^{5}F$_5$, are added according to

$$I_u^{tot} = \sum_i I_u^i \tag{5.1}$$

and

$$I_l^{tot} = \sum_i I_l^i \tag{5.2}$$

The quantitative measure of the ratio between the electrons undergoing deexcitation to (^{4}F)4p z^{5}F$_5$, n_2, and the number that deexcites further down from (^{4}F)4p z^{5}F$_5$, n_1, was derived. Intensity sums have been derived for both the current and pressure sequences.

Figure. 5.8 presents the results from the current sequence. The experiments using Ne show a significant population difference between the upper $4d$ and lower $4p$ levels. The number of electrons undergoing the $4p-4d$ and $4p-5s$ transitions is relatively constant through the sequence. As the number of $4p-4d$ and $4p-5s$ transitions in the sequence using Ar show such correlated dependence with the number of $4s-4p$ and $3d^4-4p$ transitions, it raises the question if they have same causal origin. There is no significant difference between the intensity sums of the lower and upper transitions as in the sequence using Ne. This indicates that the (^{4}F)4p z^{5}F$_5$ level is fed with electrons from enhanced $4p-4d$ and $4p-5s$ transitions.

To further investigate the relative number of electrons undergoing the $4p-4d$ and $4p-5s$ transitions with the number undergoing the $4s-4p$ and $3d^4-4p$ transitions, the fraction n_2/n_1 has been derived. As each electron emitting a photon during the above transition emits a secondary photon during its second deexcitation, $n_2/n_1 = 0$ corresponds to no electrons undergoing the $4p-4d$ or $4p-5s$ transitions and a fraction of $n_2/n_1 = 1$ means that all electrons that have populated level (^{4}F)4p z^{5}F$_5$ have originated from higher levels. The result from the derivation of these fractions are presented in Fig. 5.9.

The result from the Ne spectra show a constant ratio of approximately 5%. The low signal in the measurement with $I = 400$ mA is not as clear as in Fig. 5.8. This suggests that the low signal in the experiment had same effect on both the low and high transitions and that the effect cancels

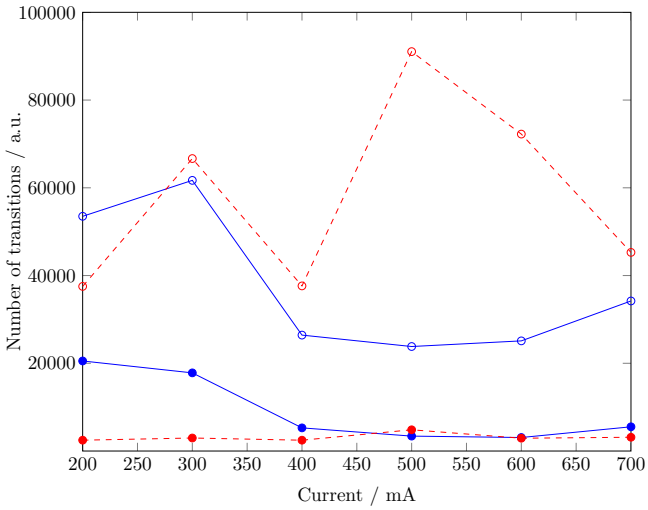

Figure 5.8: *Summation of all intensities corresponding to transitions from higher levels to $(^4F)4p\ z^5F_5$, n_2, and from $(^4F)4p\ z^5F_5$, n_1. The solid blue curves corresponds to Ar experiments and the dashed red curves to the experiments using Ne. The solid markers represents the intensity summation of all observed lines from deexcitations to $(^4F)4p\ z^5F_5$ and the curves with unfilled markers represents deexcitations from $(^4F)4p\ z^5F_5$.*

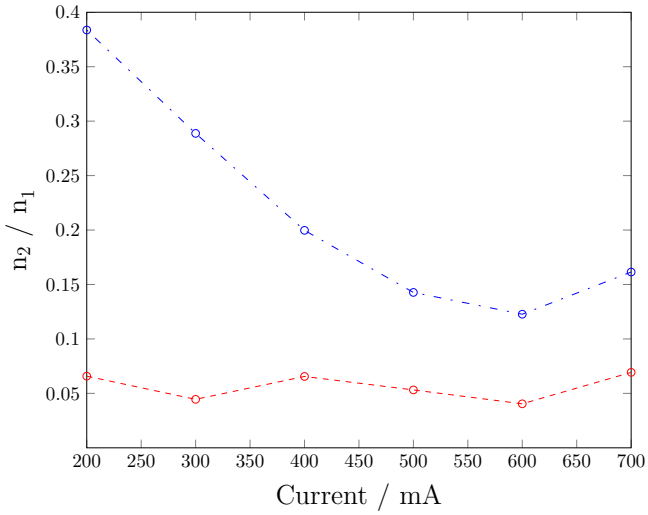

Figure 5.9: *Ratios of the number of deexcitations to and from $(^4F)4p\ z^5F_5$. The ratio plotted as a function of current describes the percentage of electrons that deexcite from a higher lying level $(^4F)4p\ z^5F_5$ relative to number of electrons that deexcite from $(^4F)4p\ z^5F_5$. The dot-dashed blue line corresponds to measurements using Ar as carrier gas and the dashed red curve describes the Ne experiments.*

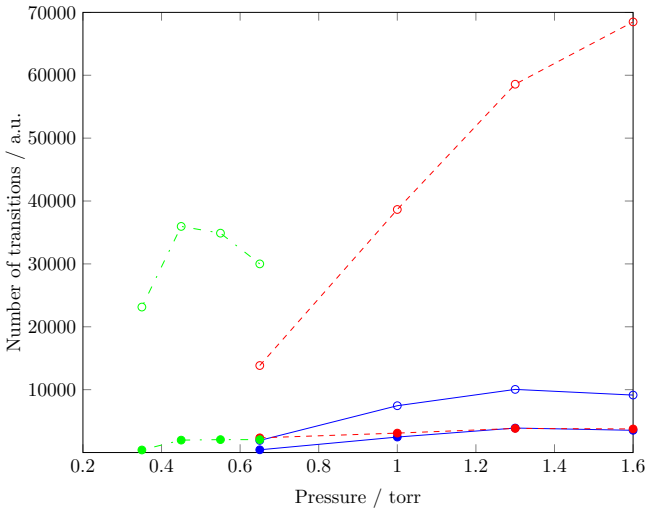

Figure 5.10: *Plot of the sum of all intensities corresponding to transitions from higher levels to* $(^4F)4p\ z^5F_5$, n_2, *and the sum of all intensities corresponding to the deexcitations from* $(^4F)4p\ z^5F_5$, n_1. *The solid blue curves corresponds to Ar experiments, the dashed red curves to the experiments using Ne and the dot-dashed green curves to the Kr experiments. The solid markers represents the intensity summation of all observed lines from deexcitations to* $(^4F)4p\ z^5F_5$ *and the curves with unfilled markers represents deexcitations from* $(^4F)4p\ z^5F_5$.

out when calculating the ratio.

The ratios from the Ar spectra present interesting results. A clear signature of overpopulation in the highly excited $4d$ levels that is rapidly growing with decreasing current is observed. The maximum ratio is found at 200 mA where approximately 40% of the electrons that have populated the intermediate level $(^4\mathrm{F})4p\ \mathrm{z}^5\mathrm{F}_5$ have initially originated from the higher $4d$ or $5s$ levels. This indicates that there is indeed some effect that efficiently populates the higher levels when using Ar and not Ne. A reasonable explanation for the overpopulation which does not include charge transfer reactions is from recombinations of V III ions. This explanation can however be ruled out as lines from higher levels have not been observed.

The result from the pressure sequence is presented in Fig. 5.10. In this figure, measurements using Kr are included and presented in green color. In the sequence using Ne, the number of electrons undergoing the $4s-4p$ and $3d^4-4p$ transitions is found to increase rapidly with increasing pressure while the number deexciting through the higher $4p-4d$ and $4p-5s$ transitions is approximately constant with pressure.

In the sequence using Kr, a significant difference between the number undergoing the high and low transition is observed. A rapid decrease in the number of upper and lower transitions is seen for $P = 0.35$ torr. Referring to the results presented in Fig. 5.6, this was expected as a consequence of the low quality of this measurement. The blue curves, corresponding to transitions from the Ar spectra, have similar shape and the relative population does not differ significantly.

Figure 5.11 presents the ratio of the results in Fig. 5.10. The relative number of $4p-4d$ and $4p-5s$ transitions are low using Kr as carrier gas. The relative population does however show a minor increase with pressure and approaches the maximum ratio of approximately 7% for $P = 0.65$ torr. The ratio using Ne on the other hand, decreases with increasing pressure from $17-5\%$. As in

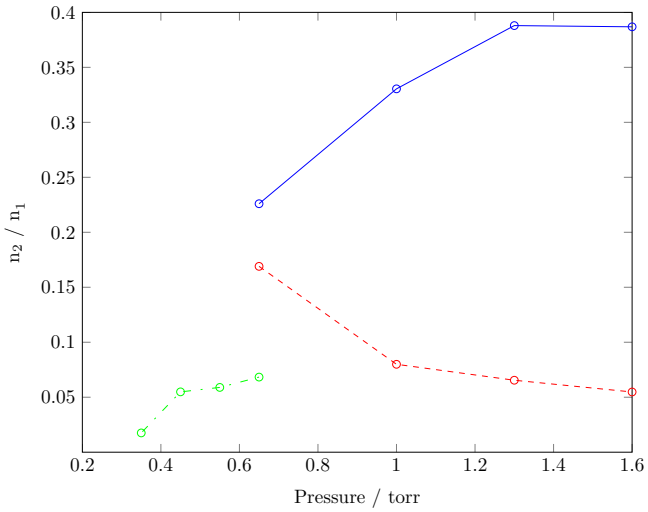

Figure 5.11: *Plot of relative populations from all deexcitations to and from* $(^4F)4p\ z^5F_5$. *The solid blue line corresponds to measurements using Ar, the dashed red curve to the Ne experiments and the dot-dashed green curve to the Kr experiments.*

the current sequence, the Ar experiments show clear signs of overpopulation. The sequence show a rapid increase with pressure with a ratio of approximately 40% for $P \geq 1.3$ torr. It should be noted that the experiments using Kr was run with $I = 200$ mA while the Ne and Ar experiments was run with $I = 300$ mA.

5.2.4 Energy difference dependence

The last part of the line enhancement investigation included an analysis of possible population dependence on the energy difference between the quintet levels in V II and the two levels in the ground configuration $3s^23p^5$ in Ar II, with $^2P_{3/2}$ at $E = 0$ and $^2P_{1/2}$ at $E = 1431.58$ cm^{-1}(Kramida et al., 2013). The result from the analysis is presented in Fig. 5.12. The negative energy difference is defined as energy of the quintet levels in V II being greater than the levels in Ar II. The data points relate to the levels in $(^4F)4d\ e^5P$, e^5F, and e^5G. As the energy difference is compared to two levels in Ar II, the data are presented with one upper and one lower x-axis corresponding to the difference from the $^2P_{3/2}$ and the $^2P_{1/2}$, respectively.

The result in Fig. 5.12 show clearly that the enhancement is dependent on ΔE. As the enhancements follow the prediction of charge transfer reactions (Johansson & Litzén, 1978) and as such reactions between levels with negative ΔE are expected to be inefficient compared to reactions with positive ΔE, the enhancement is likely caused by resonant charge transfer with the $3d^23p^5$ $^2P_{1/2}$ level in Ar II. The plotted data indicates a linear dependence but the energy interval only stretches for ~ 1000 cm^{-1}, corresponding to ~ 0.1 eV, which is small compared to the 2 eV interval investigated by Johansson & Litzén (1978).

5.3 Oscillator strengths

The results from the line enhancement investigations indicated that Ar was the most efficient choice of carrier gas when measuring branching fractions of the levels $(^4F)4d\ e^5P$, e^5F, and e^5G. As experiments using Ar showed significant overpopulation of the quintet levels using low current and high pressure, high SNR was obtained for transitions from these levels. Although the results from

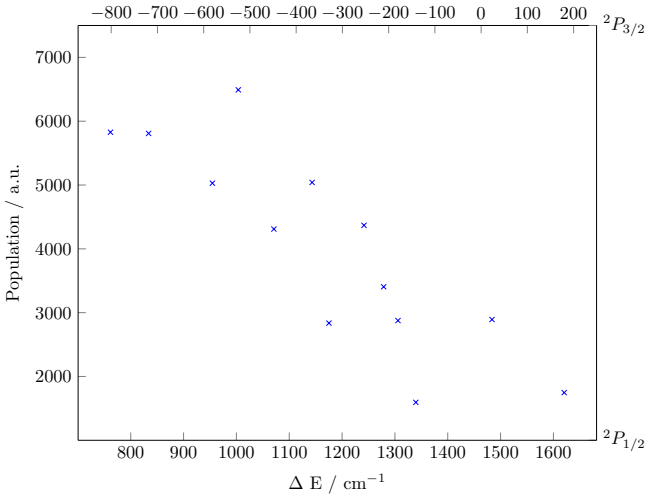

Figure 5.12: *Population as a function of energy difference between the levels in e^5F, e^5P and e^5G in V II and the two ground state levels $3s^23p^5\ ^2P_{3/2,1/2}$ in Ar II. The lower x-axis represents ΔE relative $3s^32p^5\ ^2P_{1/2}$ and the upper relative $3s^23p^5\ ^2P_{3/2}$*

the current sequence suggested the HCL to run at 200 mA, the SNR was higher with $I = 300$ mA and $P = 1.6$ torr. The experimentally derived $\log gf$ values from the recorded spectrum is presented in Table 5.4 and a comparison with theoretical calculations by Kurucz (1993) is presented in Fig. 5.13. The experimentally derived $\log gf$ values are in good agreement with the theoretical calculations (Kurucz, 1993) for strong lines but as seen in Fig. 5.13, the experimentally derived values are generally larger than the theoretical calculations. This is expected as the measured lifetimes are shorter than the theoretical and since transition probabilities are inversely proportional to the lifetime. Two strong lines was found to deviate significantly from the theoretical values. These lines corresponds to the (^{4}F)4d e^5P$_3$-(^{4}F)4p z^5D$_4$ and (^{4}F)4d e^5G$_4$-(^{4}F)4p z^3D$_3$ transitions.

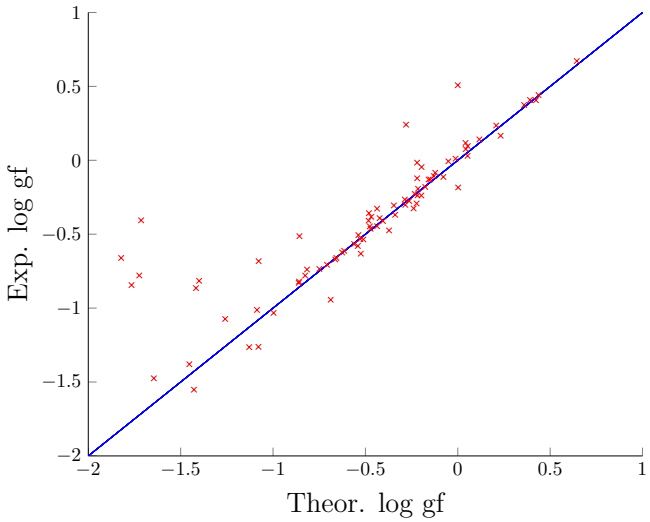

Figure 5.13: *Comparison of the experimentally obtained* $\log gf$ *values with theoretical* $\log gf$*.* (Kurucz, 1993)

Table 5.4: *Experimental results*

Upper level	Lower level	λ (Å)	σ (cm^{-1})	Exp. BF	Theor. BF	Exp. gf	Unc. (% in gf)
$(^4F)4d\ e^5P_1$	$(^4F)4p\ z^5D_0$	2831.4851	35317.155	0.224	0.205	0.415	10
	$(^4F)4p\ z^5D_1$	2836.1422	35259.162	0.401	0.417	0.742	10
	$(^4F)4p\ z^5D_2$	2844.9875	35149.538	0.265	0.269	0.495	10
	Residual:			0.110			

Upper level	Lower level	λ (Å)	σ (cm^{-1})	Exp. BF	Theor. BF	Exp. gf	Unc. (% in gf)
$(^4F)4d\ e^5P_2$	$(^4F)4p\ z^5F_2$	2777.6707	36001.387	0.029	0.023	0.084	10
	$(^4F)4p\ z^5F_1$	2799.5721	35719.744	0.055	0.008	0.166	10
	$(^4F)4p\ z^3D_2$	2806.3232	35633.814	0.038	0.083	0.114	10
	$(^4F)4p\ z^3D_3$	2819.2865	35469.967	0.155	0.231	0.472	10
	$(^4F)4p\ z^5D_1$	2823.6252	35415.464	0.078	0.095	0.238	10
	$(^4F)4p\ z^5D_2$	2832.3929	35305.835	0.266	0.300	0.824	10
	$(^4F)4p\ z^5D_3$	2844.6001	35154.325	0.310	0.237	0.964	10
	Residual:			0.069			

Upper level	Lower level	λ (Å)	σ (cm^{-1})	Exp. BF	Theor. BF	Exp. gf	Unc. (% in gf)
$(^4F)4d\ e^5P_3$	$(^4F)4p\ z^3D_3$	2800.8028	35704.049	0.097	0.230	0.428	10
	$(^4F)4p\ z^5D_2$	2813.7362	35539.933	0.022	0.041	0.097	10
	$(^4F)4p\ z^5D_3$	2825.7843	35388.405	0.105	0.180	0.471	10
	$(^4F)4p\ z^5D_4$	2826.6202	35377.939	0.718	0.492	3.219	9
	Residual:			0.058			

Upper level	Lower level	λ (Å)	σ (cm^{-1})	Exp. BF	Theor. BF	Exp. gf	Unc. (% in gf)
(^{4}F)4d e^5F$_1$	(^{4}F)4p z^5G$_2$	2614.6136	38246.568	0.093	0.092	0.151	9
	(^{4}F)4p z^3D$_1$	2751.0334	36349.977	0.368	0.399	0.660	9
	(^{4}F)4p z^5F$_2$	2765.0412	36165.826	0.161	0.183	0.292	9
	(^{4}F)4p z^5F$_1$	2786.7024	35884.706	0.113	0.049	0.208	9
	(^{4}F)4p z^5D$_0$	2806.0037	35637.872	0.117	0.127	0.219	9
	(^{4}F)4p z^5D$_1$	2810.5778	35579.871	0.098	0.102	0.184	9
	Residual:			0.050			

Upper level	Lower level	λ (Å)	σ (cm^{-1})	Exp. BF	Theor. BF	Exp. gf	Unc. (% in gf)
(^{4}F)4d e^5F$_1$	(^{4}F)4p z^5G$_2$	2601.8267	38434.535	0.206	0.204	0.543	9
	(^{4}F)4p z^5G$_3$	2612.2237	38281.560	0.135	0.131	0.357	9
	(^{4}F)4p z^3D$_1$	2736.8802	36537.952	0.080	0.106	0.234	9
	(^{4}F)4p z^5F$_2$	2750.7440	36353.800	0.262	0.294	0.771	9
	(^{4}F)4p z^5F$_3$	2769.4607	36108.113	0.072	0.076	0.213	9
	(^{4}F)4p z^3D$_2$	2778.8430	35986.199	0.102	0.048	0.307	9
	(^{4}F)4p z^5D$_1$	2795.8088	35767.824	0.049	0.047	0.148	9
	Residual:			0.094			

Upper level	Lower level	λ (Å)	σ (cm^{-1})	Exp. BF	Theor. BF	Exp. gf	Unc. (% in gf)
(^{4}F)4d e^5F$_3$	(^{4}F)4p z^5G$_3$	2604.1267	38400.589	0.145	0.154	0.530	8
	(^{4}F)4p z^5G$_4$	2617.8158	38199.784	0.135	0.145	0.500	8
	(^{4}F)4p z^5F$_2$	2741.7664	36472.837	0.082	0.108	0.335	8
	(^{4}F)4p z^5F$_3$	2760.3618	36227.134	0.416	0.405	1.719	8
	(^{4}F)4p z^3D$_2$	2769.6843	36105.197	0.037	0.010	0.153	8
	(^{4}F)4p z^5F$_4$	2778.1016	35995.803	0.063	0.071	0.263	8
	(^{4}F)4p z^3D$_3$	2782.3055	35941.416	0.033	0.009	0.137	8
	(^{4}F)4p z^5D$_2$	2795.0719	35777.254	0.064	0.067	0.271	8
	(^{4}F)4p z^5D$_3$	2806.9550	35625.793	0.013	0.018	0.054	8
	Residual:			0.012			

Upper level	Lower level	λ (Å)	σ (cm^{-1})	Exp. BF	Theor. BF	Exp. gf	Unc. (% in gf)
(^{4}F)4d e^5F$_4$	(^{4}F)4p z^5G$_3$	2595.1366	38533.616	0.006	0.008	0.028	6
	(^{4}F)4p z^5G$_4$	2608.7332	38332.781	0.155	0.156	0.743	6
	(^{4}F)4p z^5G$_5$	2625.6204	38086.236	0.132	0.132	0.642	6
	(^{4}F)4p z^5F$_3$	2750.2639	36360.147	0.147	0.147	0.781	6
	(^{4}F)4p z^5F$_4$	2767.8749	36128.800	0.441	0.445	2.367	6
	(^{4}F)4p z^5F$_5$	2783.4260	35926.947	0.036	0.038	0.197	6
	(^{4}F)4p z^5D$_3$	2796.5189	35758.742	0.071	0.063	0.071	6
	Residual:			0.012			

Upper level	Lower level	λ (Å)	σ (cm^{-1})	Exp. BF	Theor. BF	Exp. gf	Unc. (% in gf)
(^{4}F)4d e^5F$_5$	(^{4}F)4p z^5G$_5$	2616.1421	38224.222	0.170	0.174	1.026	6
	(^{4}F)4p z^5G$_6$	2636.1715	37933.799	0.097	0.103	0.592	6
	(^{4}F)4p z^5F$_4$	2757.3436	36266.789	0.186	0.183	1.247	6
	(^{4}F)4p z^5F$_5$	2772.7760	36064.939	0.407	0.436	2.764	6
	(^{4}F)4p z^5F$_4$	2786.5812	35886.267	0.085	0.096	0.579	6
	(^{4}F)4p z^3G$_5$	2958.1820	33804.546	0.051	0.003	0.393	6
	Residual:			0.004			

Upper level	Lower level	λ (Å)	σ (cm^{-1})	Exp. BF	Theor. BF	Exp. gf	Unc. (% in gf)
(^{4}F)4d e^5G$_2$	(^{4}F)4p z^5G$_2$	2611.9702	38285.275	0.148	0.150	0.406	11
	(^{4}F)4p z^5G$_3$	2622.4490	38132.295	0.015	0.014	0.042	11
	(^{4}F)4p z^3D$_1$	2748.1068	36388.687	0.169	0.472	0.511	11
	(^{4}F)4p z^5F$_2$	2762.0840	36204.547	0.117	0.130	0.358	11
	(^{4}F)4p z^5F$_3$	2780.9553	35958.866	0.095	0.104	0.293	11
	(^{4}F)4p z^5F$_1$	2783.6978	35923.439	0.289	0.223	0.900	11
	(^{4}F)4p z^5D$_1$	2807.5217	35618.602	0.099	0.100	0.312	11
	(^{4}F)4p z^5D$_2$	2816.1899	35508.969	0.057	0.052	0.183	11
	Residual:			0.011			

Upper level	Lower level	λ (Å)	σ (cm^{-1})	Exp. BF	Theor. BF	Exp. gf	Unc. (% in gf)
(^{4}F)4d e^5G$_3$	(^{4}F)4p z^5G$_3$	2617.4039	38205.795	0.159	0.180	0.578	8
	(^{4}F)4p z^5G$_4$	2631.2410	38004.881	0.039	0.005	0.143	8
	(^{4}F)4p z^5F$_2$	2756.4878	36278.049	0.162	0.257	0.655	8
	(^{4}F)4p z^5F$_3$	2775.2825	36032.367	0.095	0.099	0.388	8
	(^{4}F)4p z^3D$_2$	2784.7048	35910.448	0.318	0.276	1.310	8
	(^{4}F)4p z^5F$_4$	2793.2168	35801.016	0.059	0.061	0.244	8
	(^{4}F)4p z^3D$_3$	2797.4561	35746.762	0.053	0.004	0.218	8
	(^{4}F)4p z^5D$_2$	2810.3720	35582.478	0.082	0.083	0.344	8
	(^{4}F)4p z^5D$_3$	2822.3915	35430.945	0.022	0.025	0.093	8
	Residual:			0.011			

Upper level	Lower level	λ (Å)	σ (cm^{-1})	Exp. BF	Theor. BF	Exp. gf	Unc. (% in gf)
(^{4}F)4d e^5G$_4$	(^{4}F)4p z^5G$_4$	2623.4909	38117.150	0.191	0.224	0.984	9
	(^{4}F)4p z^5G$_5$	2640.5725	37870.575	0.006	0.006	0.034	9
	(^{4}F)4p z^5F$_3$	2766.6707	36144.525	0.255	0.387	1.466	9
	(^{4}F)4p z^5F$_4$	2784.4935	35913.173	0.130	0.135	0.755	9
	(^{4}F)4p z^3D$_3$	2788.7183	35858.766	0.298	0.117	1.742	9
	(^{4}F)4p z^5F$_5$	2800.2319	35711.328	0.028	0.033	0.166	9
	(^{4}F)4p z^5D$_3$	2813.4843	35543.115	0.074	0.073	0.439	9
	(^{4}F)4p z^5D$_4$	2814.3137	35532.641	0.009	0.018	0.055	9
	Residual:			0.009			

Upper level	Lower level	λ (Å)	σ (cm^{-1})	Exp. BF	Theor. BF	Exp. gf	Unc. (% in gf)
(^{4}F)4d e^5G$_5$	(^{4}F)4p z^5D$_5$	2629.4862	38030.242	0.187	0.204	1.072	9
	(^{4}F)4p z^5F$_4$	2772.1716	36072.802	0.402	0.399	2.560	9
	(^{4}F)4p z^5F$_5$	2787.7703	35870.960	0.185	0.177	1.191	9
	(^{4}F)4p z^5D$_4$	2801.7249	35692.297	0.213	0.208	1.385	9
	Residual:			0.013			

Upper level	Lower level	λ (Å)	σ (cm^{-1})	Exp. BF	Theor. BF	Exp. gf	Unc. (% in gf)
(^{4}F)4d e^5G$_6$	(^{4}F)4p z^5G$_6$	2630.4547	38016.241	0.374	0.398	2.548	6
	(^{4}F)4p z^5F$_5$	2766.4528	36147.372	0.623	0.599	4.698	6
	Residual:			0.003			

Chapter 6

Discussion

6.1 Line enhancements

In the pressure and current sequences using Ar as carrier gas, evidence of selective overpopulation was obtained. The overpopulation in the $(^4\mathrm{F})4d\ e^5\mathrm{P}$, $e^5\mathrm{F}$ and $e^5\mathrm{G}$ levels in V II was found to be dependent on both pressure and current. In addition, the overpopulation was observed to be dependent on energy difference between resonant levels in Ar II and V II. This follows the predictions by Johansson & Litzén (1978) and indicates that the overpopulation was caused by selective charge transfer reactions.

If the overpopulation was caused by charge transfer reactions, the observed dependency on pressure is not unexpected. The increased plasma pressure causes a shorter mean free path for the ions and atoms in the plasma and the time of acceleration of each charged particle by the external electric field therefore decreases. As no significant potential barrier must be overcome in collisions between ions and atoms, resonant charge transfer reactions do not depend on collision energy but on the number of collisions and energy difference from perfect resonance. The close encounters increase the probability of the pseudo-molecular states to form and hence also the probability of charge transfer reactions. The presented results are therefore in agreement with the prediction that the selective charge transfer reactions only depend on the number of collisions and energy difference.

However, the observed dependence on current is more unexpected. If electron collisions is the dominant process in the plasma, the high rate of electron collisions could interrupt the pseudo-molecular state. As the current decreases, the electron collisions are expected to be less significant. This could explain the increased overpopulation with decreasing current.

As the enhancements follow the prediction of charge transfer reactions, the enhancement is likely caused by resonant charge transfer with the $3d^2 3p^5\ ^2\mathrm{P}_{1/2}$ level in Ar II. The data indicate a linear dependence but the energy interval is small compared to the interval studied by Johansson & Litzén (1978). The overpopulation dependence on the energy difference could therefore be non-linear for larger energy intervals.

The measurements using Kr as carrier gas was found to cause much noise. Noise can be caused by pressure fluctuations and time varying sputtering of the cathode material. Increasing the current from a stable and equilibrated discharge can cause more sputtering and therefore increase the pressure. The pressure increase can at some point slow down and begin a rapid decrease due to plasma condensation. This oscillating effect varies depending on carrier gas, cathode material, pressure and current and for a specific carrier gas and cathode material, certain stable combinations of pressure and current exists where high quality measurements can be performed. Difficulties occur in experiments where the desired pressure and current values lies in between such stable combina-

tions and running experiments with unstable and fluctuating pressure results in spectra with much noise. As the FTS is recording an interferogram, the detection is sensitive to fluctuating intensities and thus require a stable light source.

The results from the current and pressure sequences showed that excitations to the (^{4}F)4p levels was efficiently produced using Kr. As Kr has a heavier atomic mass than Ar, the Kr ions are expected to bombard the cathode walls with higher momenta and therefore sputter more of the cathode material into the plasma.

It was further shown that the (^{4}F)4p levels in V II were efficiently populated using Ne and dependence on both pressure and current was found. The results show a rapid increase with pressure and suggested maximum at $\sim$ 450 mA. As the sputtering of the cathode material is dependent on current and pressure, the observed intensity dependence is therefore explained by an increased number of V^+ ions in the plasma. The (^{4}F)4d e^5P, e^5F and e^5G levels were found to be more populated compared to the Kr experiments but lines from these levels were detected with low SNR. No evidence of overpopulation of the (^{4}F)4d e^5P, e^5F and e^5G levels was found and the observed lines was likely caused by electron collisions. The results showed that the population ratio between the (^{4}F)4p z^5F$_5$ and the levels in (^{4}F)4d and 5s was constant with current and decreased with pressure. Increased current causes more sputtering which should increase the intensities but not affect the relative population. As the mean free path decreases with higher pressure, the number of collisions is expected to increase and the average collision energy to decrease. The observed decrease of the population ratio with increasing pressure could thus be explained by the decreased mean free path of the electrons.

The discharge was found stable using Ne and more stable combinations of current and pressure could therefore be used. This suggests that Ne could be an efficient gas to investigate selective charge transfer reactions for other ions. As the ground state in Ne^+ is higher than in Ar^+, it could be used to overpopulate highly excited states in Cr^+, Mn^+, Fe^+, Co^+, or other metal ions with higher ionization limits.

6.2 Oscillator strengths

As the (^{4}F)4d e^5P, e^5F and e^5G levels in V II could be overpopulated using selective charge transfer with Ar^+ ions, oscillator strengths of 79 lines was derived. As the experimental $\log gf < -1$ deviated significantly from the theoretical, these values need confirmation. The difference between the strong (^{4}F)4d e^5P$_3$-(^{4}F)4p z^5D$_4$ and (^{4}F)4d e^5G$_4$-(^{4}F)4p z^3D$_3$ transitions can either be a result of inaccurate theoretical calculations or caused by blends from unidentified lines.

Chapter 7

Conclusion

In this thesis, evidence of overpopulation in the (^{4}F)4d e^5P, e^5F and e^5G levels in V II was observed using Ar gas in the HCL. The overpopulation was found to be sensitive to current and pressure and the results showed a clear enhancement increase with pressure and linear increase with decreasing current.

In addition, the overpopulation in the (^{4}F)4d e^5P, e^5F and e^5G levels was found to be dependent on the energy difference from perfect resonance with the ground configuration in Ar II. This indicates that the overpopulation was caused by selective charge transfer reactions and the results are in agreement with previous charge transfer investigations using hollow cathodes.

The results in this thesis and from previous charge transfer investigations suggest that selective charge transfer reactions can enable branching fraction measurements of highly excited states in metal ions. Experiments using Ne showed no enhancements in V II but as Ne II has no levels in resonance with the quintet terms, this was expected. However, the experiments were found to cause a stable discharge and Ne could therefore be used to investigate charge transfer reactions in other metal ions.

Through controlled overpopulation of the (^{4}F)4d e^5P, e^5F and e^5G levels in V II, branching fractions measurement was enabled and experimental $\log gf$ values of 79 lines was derived. The derived $\log gf$ values were in agreement with theoretical calculations (Kurucz, 1993) for $\log gf > -1$ but show discrepancy for lower values.

In conclusion, this thesis successfully demonstrates a method to measure branching fraction of highly excited states in metal ions through selective overpopulation and a thorough investigation of current and pressure dependence of V II using Ar, Ne and Kr as carrier gas.

References

Bransden, B., & McDowell, M. 1992, Charge Exchange and the Theory of Ion-Atom Collisions (Oxford University Press)

Engström, L. 1998, Lund Reports on Atomic Physics (LRAP), 232, Available online at: `http://kurslab-atom.fysik.lth.se/Lars/GFit/Html/index.html` [2014, May 19]

Gray, C. F. 2005, The Observations and Analysis of Stellar Photospheres (Cambridge University Press, New York)

Johansson, S., & Litzén, U. 1978, Journal of Physics B: Atomic, Molecular and Optical Physics, 11 L703

Kramida, A. E., Ralchenko, Y., Reader, J., & NIST ASD Team. 2013, NIST Atomic Spectra Database (ver. 5.1), Available online at: `http://physics.nist.gov/asd` [2014, May 18]. National Institute of Standards and Technology, Gaithersburg, MD.

Kurucz, R. L. 1993, Data available online at: `http://www.pmp.uni-hannover.de/cgi-bin/ssi/test/kurucz/sekur.html`, [2014, May 19]

Litzén, U. 2003, Introduction to Fourier Transform Spectroscopy, (Lund Observatory, Lund University)

Nave, G., Sansonetti, C. J., & Griesmann, U. 1997, Opt. Soc. Am. Tech. Digest Series 3, Fourier Transform Spectroscopy: Methods and Applications. Opt. Soc. Am., Washington, DC, p. 38

Salit, M., Travis, J., & Winchester, M. 1996, Applied Optics

Sikström, C., Nilsson, H., Litzén, U., Blom, A., & Lundberg, H. 2002, Journal of Quantitative Spectroscopy and Radiative Transfer, 74, 355

Taylor, B. N., & Kuyatt, C. E. 1994, Guidelines for Evaluating and Expressing the Uncertainty of NIST Measurement Results, Tech. rep., NIST Tecnical Note 1297

Thorne, A. P., Litzén, U., & Johansson, S. 1999, Spectrophysics - Principles and applications (Springer-Verlag Berlin Heidelberg)

Whaling, W., Anderson, W. H. C., Carle, M. T., Brault, J. W., & Zarem, H. A. 1995, Journal of Quantitative Spectroscopy and Radiative Transfer, 53, 1